CHALMERS
UNIVERSITY OF TECHNOLOGY

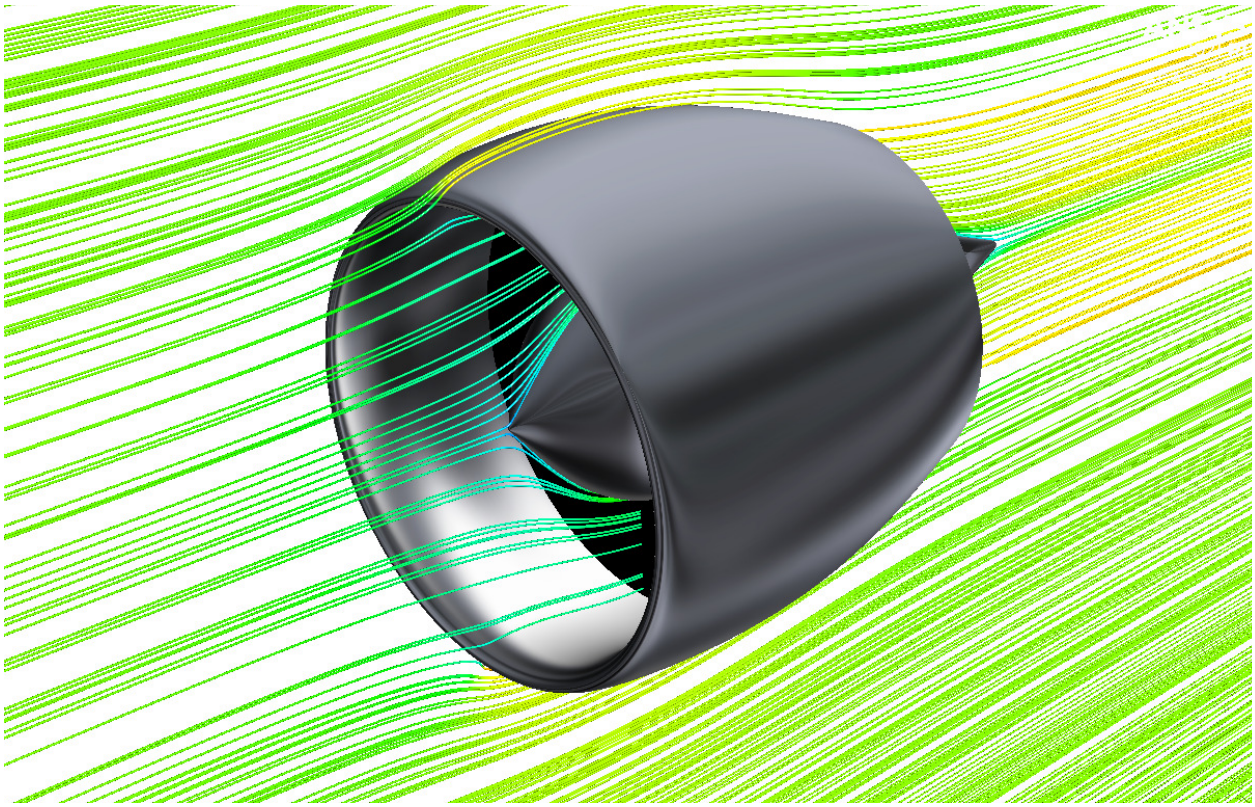

Multi-point aerodynamic design and optimization of a nacelle for an electric fan

Master's thesis in Applied Mechanics

ARAVINDHAN VENKATESH

DEPARTMENT OF MECHANICS AND MARITIME SCIENCES
CHALMERS UNIVERSITY OF TECHNOLOGY
Gothenburg, Sweden 2022
www.chalmers.se

MASTER'S THESIS 2022

Multi-point aerodynamic design and optimization of a nacelle for an electric fan

ARAVINDHAN VENKATESH

CHALMERS
UNIVERSITY OF TECHNOLOGY

Department of Mechanics and Maritime Sciences
Division of Fluid Dynamics
CHALMERS UNIVERSITY OF TECHNOLOGY
Gothenburg, Sweden 2022

Multi-point aerodynamic design and optimization of a nacelle for an electric fan
ARAVINDHAN VENKATESH

Supervisors: Marcus Lejon, GKN Aerospace AB, Sweden
Vinícius Tavares Silva, Chalmers University of technology

Co-supervisor: Anders Lundbladh, GKN Aerospace AB, Sweden

Examiner: Carlos Xisto, Department of Mechanics and Maritime Sciences

Master's Thesis 2022
Department of Mechanics and Maritime Sciences
Division of Fluid Dynamics
Chalmers University of Technology
SE-412 96 Gothenburg
Telephone +46 31 772 1000

Typeset in LaTeX
Department of Mechanics and Maritime Sciences
Gothenburg, Sweden 2022

Multi-point aerodynamic design and optimization of a nacelle for an electric fan
ARAVINDHAN VENKATESH
Department of Mechanics and Maritime Sciences
Chalmers University of Technology

Abstract

Engines that power commercial airliners are becoming more carbon neutral as propulsion technologies are evolving at a rapid pace, targeting progressive decarbonization goals. Electrification of sub-regional aircraft could be an initial step in controlling emissions in the skies. In accordance with this goal, GKN Aerospace has been leading the EleFanT project that is aimed at developing an electric fan thruster for an electric aircraft. The present multi-point aerodynamic design of the nacelle is done as a part of the Electric Fan thruster (EleFanT) project. A multi-objective shape optimization method was implemented to obtain an initial set of axisymmetric shape parameters for nacelle and nozzle geometries. The optimization workflow consists of a non-dominated sorting genetic algorithm (NSGA-II), coupled with 2-D axisymmetric Reynolds Averaged Navier Stokes (RANS) equations based CFD code. The good designs from 2-D cruise studies were subjected to multi-point analysis, where the 3-D asymmetric flow fields from various operating points like cruise, take-off and crosswind were studied. The aerodynamic drag and thrust coefficients and the engine performance metrics were recorded using a defined bookkeeping method. For the 3-D simulations, a validated fan-inlet coupling model, the modified parallel compressor (MPC) method was employed at the fan face boundary to adapt to the incoming flow distortions. Thorough investigations on inlet drooping were done to analyze its positive impact on intake aerodynamics. With drooping, besides a reduction in drag coefficient C_d at cruise, mitigation of intake flow separation and distortion at take-off was also achieved. Further, a small increment done to the highlight radius at the lower position of the nacelle gave sizeable reductions in incoming flow distortion at the fan face.

Keywords: aerodynamic design, multi-objective optimization, nacelle design, multi-point analysis, CFD.

Acknowledgements

The thesis work was carried out at Chalmers Division of Fluid Dynamics in close collaboration with GKN Aerospace AB. I extend my sincere gratitude to my supervisors, Vinícius Tavares Silva from Chalmers University and Marcus Lejon from GKN Aerospace, for their extended support, guidance, and technical information that helped me in accomplishing the project. I am very thankful to my co-supervisor, Anders Lundbladh, who enlightened me on several occasions regarding flow physics and design selection.

I would also like to thank my examiner, Carlos Xisto, for his timely help during the entire project.

Aravindhan Venkatesh, Gothenburg, August 2022

List of Acronyms

Below is the list of acronyms that have been used throughout this thesis listed in alphabetical order:

AoA	Angle of Attack
BPR	Bypass ratio
CFD	Computational Fluid Dynamics
CST	Class-Shape Transformation
CW	Crosswind
EA	Evolutionary Algorithm
FPR	Fan Pressure Ratio
GA	Genetic Algorithm
IPR	Intake Pressure Recovery
MFCR	Mass Flow Capture Ratio
MHB	Maximum Half Breadth
MOO	Multi-Objective Optimization
MPC	Modified Parallel Compressor
NACA	National Advisory Committee for Aeronautics
NSGA-II	Non-dominated Sorting Genetic Algorithm-II
OGV	Outlet Guide Vane
PEMFC	Proton Exchange Membrane Fuel Cell
RANS	Reynolds Averaged Navier Stokes Equation
SAF	Sustainable Aviation Fuel
TO	Take-off

Nomenclature

Below is the nomenclature of indices, reference frame definition, parameters, and variables that have been used throughout this thesis.

Indices and reference frame

i,j,k	Subscripts used in the velocity and normal vectors
∞	Subscript for free stream properties
1,2	Subscripts to represent fan face inlet and fan OGV outlet plane properties
i	Superscript to denote a fan face cell
x,y,z	Coordinates in the Cartesian reference frame
ξ,ψ	Radial and axial coordinates unitized with the chord length

Parameters

η_{is}	Isentropic efficiency
η_i	Intake pressure recovery
c_{dis}	Discharge coefficient
c_{th}	Thrust coefficient
DC_{60}	Flow distortion parameter
F_n	Net propulsive force
T_N	Standard net thrust
ϕ_{pre}	Pre-entry force
ϕ_{FC}	fan cowling force
c_d	Drag coefficient
c_d^*	Normalized drag coefficient
Φ	Azimuthal angles
c_p	Pressure coefficient

θ_d	Inlet drooping angle
PR_{fan}	Fan pressure ratio
$\dot{m}$	Engine mass flow
γ	Ratio of specific heats

Variables

ρ	Fluid density
u_i	Velocity component in Cartesian coordinates
$\mathbf{U}$	Velocity vector
P,P_t	Static and stagnation pressures
T ,T_t	Static and stagnation Temperatures
M	Mach number
AoA	Flow angle of attack

Contents

List of Figures

List of Tables

1

Introduction

1.1 Towards a sustainable aviation

The current trends in commercial aviation aim at making engines more compact and reducing emissions. Further, ambitious goals for future air transportation in terms of perpetuating lowered CO_2 emissions in the skies and achieving net zero carbon emissions by 2050 have been set by the European aviation industry. Aspects addressed include advancements in aircraft components; improvements in aircraft control and air traffic management, and sustainable aircraft fuels (SAF). Figure 1.1 is a pictorial representation of the 2050 aviation fuel budget goal. Almost 90% of aviation fuel is expected to be from renewable sources [1]. Presently, aircraft emissions have a minor contribution to the elevated global effects, with cruise operations accounting for three-fourths of total emission [2]. The countermeasures include sustainable energy sources for engines, innovative aircraft architectures and plausible environmental regulations [3]. Presently, commercial airliners, being dependent on fossil fuels, continue to be a significant contributor of greenhouse gases in the skies, that account for 3% of net emissions, particularly CO_2 and NO_X [4]. Although, aero-engine manufacturers are working on emission mitigation through efficient combustion analysis [5], electrification of short-range commercial aircrafts powered by batteries or H_2 fuel cells may serve as an initial step in the de-carbonization goal.

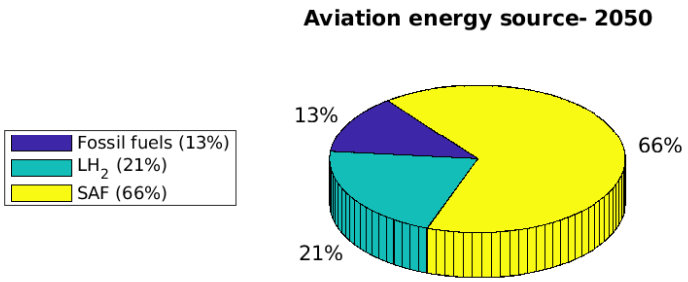

Figure 1.1: Breakdown of expected aviation fuel sources by 2050

1.2 H_2 fuel cells in aviation and the present work scope

Emergence of hybrid-electric aircraft propulsion systems plays a key role in reducing emissions compared to conventional engines in light aviation category. The feasibility in introducing full electric propulsion system in long-range maneuvers is limited by present battery technology and limited research sources [6]. Presently, much research work is being done on hydrogen fuel cells as an alternative to batteries in various classes of aircrafts [7, 8]. With a fuel cell powered drive or a hybrid drive comprised of batteries and fuel cells can result in enhanced range, payload capabilities and reduced energy utilization [9]. Further, LH_2 propulsion has been estimated to have a low environmental impact. Specifically, polymer electrolyte membrane fuel cells (PEMFCs) are tested to be more compatible for aerospace applications with reduced environmental impact [9]. The present work is an aspect of the GKN Aeropsace's EleFanT project that deals with a standalone nacelle design for an electric aircraft intended for sub-regional commercial air transportation. The project is in collaboration with Universities in Sweden, aimed at reducing CO_2 emissions in the skies [10].

1.3 Aerodynamic profiles-Nacelle design

1.3.1 Theory of nacelle design

Nacelle design is challenging as it involves balancing weight and aerodynamic performance under a range of operating conditions encountered during a flight profile [11]. A lot of design methods have been formulated and validated by various authors, among which, owing to the fact that the nacelle design has to satisfy conflicting parameters, a multi-objective problem formulation has been widely used [12]. The current modern civil-aero engines are adapted to work at high bypass rati (BPR) and reduced fan pressure ratio (FPR) to facilitate increased propulsion efficiency and reduced fuel consumption [13]. With increased fan diameter, the nacelle possesses a larger wetted area A_{wetted} and weight thus increasing the total viscous drag and installation drag [12]. The wetted area A_{wetted} is the total surface area of all the nacelle component surfaces considered in the present study. Intuitively, this has resulted in considering short inlets and exhaust lengths, with the aim of reducing the total surface area and, eventually, the weight of the nacelle. However, these designs suffer from high susceptibility to fan distortions when flow approaches at an AoA due to the insufficiency of intake length to straighten the flow. This effect of having flow separation induced by the intake portion can lead to a fan stall [14, 13]. These aforementioned counteracting effects make nacelle design optimization a challenging task.

A design approach used in the nacelle optimization process includes the natural laminar flow control method, where the flow over the cowling is made to relatively stay in the laminar flow region in order to reduce the drag force [15]. In the present study, a parameterized design approach is used based on pre-determined geometric constraints, and the nacelle's configuration drag is deduced from the

net thrust and the propulsive force.

1.3.2 Nacelle profile optimization approaches and previous work

In this section, the design optimization approaches used by various authors to optimize nacelle profile are discussed in brief. The two majorly used methods are as follows:

- **Parametric design optimization:** The parametric design optimization method is a widely used approach to optimize aerodynamic profiles that are bound to design objectives or objective functions. Since the aerodynamic profiles are essentially parameterized, it is easier to alter the parameter set in an iterative manner until an optimal set of design parameters is obtained based on the considered aerodynamic performance parameters. This method is used in the present study for the aerodynamic design of nacelle and nozzle profiles.
- **Inverse design method:** As the name suggests, this method uses an iterative inverse workflow that alters the geometry of the aerodynamic profile as a function of the difference between the pressure distribution from the current evaluation and the desired pressure distribution. The initial design along with the free-stream flow field is used to deduce the residual pressure difference in each iteration, that helps the algorithm to calculate the geometry difference in the successive iteration [16].

1.3.3 Parameterized curve generation method

The curve parametrization for the aerodynamic profile generation is required to be mathematically well-posed, easy to control, and to have the least number of control parameters that define the profile. A robust class-shape transformation (CST) method was employed for generating aerodynamic nacelle and nozzle profiles based on geometric constraints. The CST method was validated by various authors in their works related to aerodynamic shape optimization of nacelle profiles and was also proven to generate aerodynamically intuitive designs.

1.3.4 Multi-objective optimization study

A parameterized shape optimization method is used in the present study to search for feasible evaluations in the design space. Various studies have been performed on multi-objective optimization (MOO) of aerodynamic profiles building surrogate models, that helped in quick convergence of the optimizer [17]. In the present work, an MOO study on nacelle and nozzle geometry was carried out with a fast Non-dominated sorting genetic algorithm-II (NSGA-II). It was shown that the novelty in the optimizer helps with better non-dominated sorting at the onset of the optimization and quicker convergence towards the end of the process [18]. The considered multi-level NSGA-II optimizer was shown to have performed well in optimizing a standalone nacelle profile [12]. In the current study, the optimization process was started off with an initial set of designs from a Latin

hypercube sampling, that drives the optimization process and to facilitate a better sweep of the design space.

1.4 Objectives of the thesis work

The objectives of the present work include the following

- Perform mesh validation studies and selection of appropriate boundary conditions for the fan inlet, OGV exit plane and the computational domain boundaries to be used in 2-D and 3-D computational analysis.
- To conduct 2-D axisymmertic, multi-objective design optimization studies of a nacelle and nozzle profile based on a genetic algorithm and CFD solution and to choose the best design/designs for further asymmetric analysis.
- To conduct 3-D computational analysis for chosen designs and select one design based on aerodynamic performance parameters considering cruise operating condition.
- To analyze the effects of geometric profile modification on the flow field and to validate the nacelle's multi-point operation capabilities.
- To incorporate a fan-inlet coupling model called the modified parallel compressor (MPC) method for multi-point operation. Each operation point has its own fan performance curves and design operation points.

2

Theory

2.1 Isentropic flow relations and mass flow equations for compressible flow

Figure 2.1 shows the station numbering convention used to establish the isentropic flow relations for setting up the boundary conditions for the preliminary simulations. The **farfield** zone features an unperturbed flow field approaching axially with a Mach number M_∞, which is the flight Mach number. The flight altitude can be used to deduce far-field static pressure P_∞ and temperature T_∞ using the following relations.

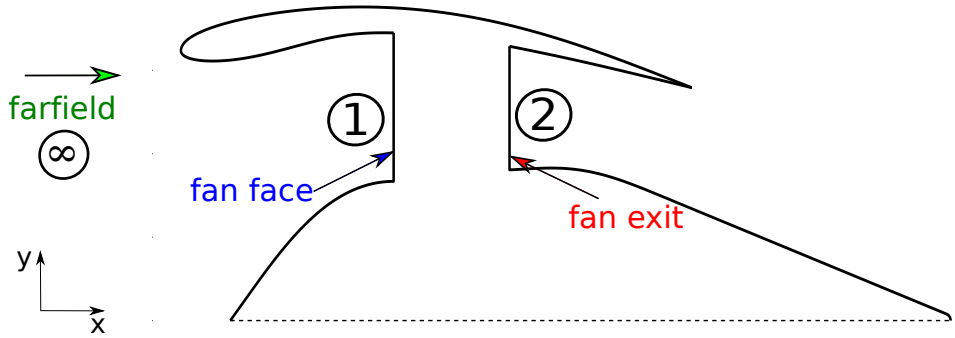

Figure 2.1: Description of nacelle station points.

$$P_\infty = P_{std}(1 - 0.065H/288.15)^{5.2561} \tag{2.1}$$

$$T_\infty = 288.15 - 0.0065H + dT_{ISA} \tag{2.2}$$

With the flight Mach number M_∞, the far-field stagnation pressure and temperature are deduced from the following isentropic compressible flow relations.

$$P_{t\infty} = P_\infty \left(1 + \frac{\gamma - 1}{2} M_\infty^2\right)^{\frac{\gamma}{\gamma - 1}} \tag{2.3}$$

$$T_{t\infty} = T_\infty \left(1 + \frac{\gamma - 1}{2} M_\infty^2\right) \tag{2.4}$$

Assuming ideal gas formulation, the fluid density at station 0 and corresponding far-field velocity are estimated from the relations below.

$$\rho_\infty = \frac{P_\infty}{RT_\infty} \qquad u_\infty = M_\infty \sqrt{\gamma R T_\infty} \tag{2.5}$$

Where, $\dot{m}$ is the design mass flow through the engine. The inlet stream-tube capture area A_∞ is deduced from the following relation.

$$A_\infty = \frac{\dot{m}}{\rho_\infty u_\infty} \tag{2.6}$$

The mass flow capture ratio (MFCR) is one of the inlet parameters that determines the intake performance of the nacelle, and it is defined as the ratio of inlet stream tube area to the highlight area (MFCR = A_∞ / A_{hi}). Preferably, for cruise operation in a turbofan engine, an optimal MFCR in the range of 0.7-0.75 is desirable so as to balance the pre-entry drag (ϕ_{pre}) from the intake stream tube and the lip suction force from the cowl intake. A very low MFCR causes excessive flow acceleration around the lip, consequently increasing spillage for low AoA flows

The fan face and the outlet guide vane (OGV) exit plane boundaries are depicted as stations 1 and 2 in Fig. 2.1.

$$P_{t1} = P_{t\infty}\eta_i \tag{2.7}$$

Where, η_i is the intake total pressure recovery, which is taken to be 0.998 in the current study. Average Mach number M_1 at fan face is obtained from the Q-function deduced at station 1 from the corresponding flow properties.

$$\dot{m} = P_{t1}\sqrt{\frac{\gamma}{RT_{t1}}}A_{ff}M_1\left(1+\frac{\gamma-1}{2}M_1^2\right)^{-\frac{(\gamma+1)}{2(\gamma-1)}} \tag{2.8}$$

The flow through the intake is isentropic, hence the total temperature at fan face is same as fan face total pressure.

$$P_1 = P_{t1}\left(1+\frac{\gamma-1}{2}M_1^2\right)^{-\frac{\gamma}{\gamma-1}} \tag{2.9}$$

$$T_1 = T_{t1}\left(1+\frac{\gamma-1}{2}M_1^2\right)^{-1} \tag{2.10}$$

The total pressure and total temperature at station 2, fan exit is estimated with the fan pressure ratio PR_{fan} and fan isentropic efficieny η_{is}.

$$P_{t2} = P_{t1}PR_{fan} \tag{2.11}$$

$$T_{t2} = T_{t1}\left(1+\frac{1}{\eta_{is}}\left(PR_{fan}^{\frac{\gamma-1}{\gamma}}-1\right)\right) \tag{2.12}$$

$$P_2 = P_{t2}\left(1+\frac{\gamma-1}{2}M_2^2\right)^{-\frac{\gamma}{\gamma-1}} \tag{2.13}$$

$$T_2 = T_{t2}\left(1+\frac{\gamma-1}{2}M_2^2\right)^{-1} \tag{2.14}$$

the total and static properties at stations 1 and 2 can be used as inputs in the CFD solver and also to deduce the aerodynamic performance parameters.

2.2 Thrust and drag bookkeeping

Many approaches have been developed to estimate drag and other forces on an aerodynamic body from a discretized computational domain with solution field obtained from Reynold's averaged Navier Stokes equation (RaNS) based models [19]. The principle drag components on an aerodynamic body fall into the following categories.

1. **Viscous or profile drag :** The profile drag is the summation of skin friction forces on the surface and form drag. The latter part contributes to overall drag owing to the modification of pressure fields around the body, while the former part is the tangential force acting on the surface due to velocity gradient stemming from flow shear.
2. **Induced drag :**An important aspect in a lift-producing body is the modification of the span-wise velocity profile due to vortices. This transforms the effective lift vector as a result of flow modification, resulting in an additional drag component.
3. **Wave drag :** In bodies moving at transonic or supersonic speeds, the presence of shock waves can lead to higher drag as a result of an abrupt change in the flow field and shock induced separation.

2.2.1 Drag estimation methodologies

Theoretically, two drag estimation methodologies can be employed, viz., body-based perspective and flow-based perspective. In the body-based perspective, the forces on the body are estimated from the near-field pressure and shear stress components obtained around the aerodynamic body in the following manner.

$$F_i = \iint_S \left(-p_i + \tau_{ij} n_j\right) dS \tag{2.15}$$

Where, τ_{ij} represents the total stress tensor accounting for both viscous and laminar terms and n_j is the surface normal vector in indical notation. In the case of a flow based perspective, linear force balance equations in the principle directions are applied over the bounding surfaces 'S' that enclose a defined steady-flow control volume.

$$\sum F_b^i = \iint_S \left(\rho U_i (U_j n_j)\right) dS \tag{2.16}$$

Here, F_b^i denotes the summation vector of all body forces present within the control volume. V_i represents the velocity vector at any given location in the flow field, and n_j is the surface normal vector. Considering a closed control volume containing an aerodynamic body, the surface integration of the term $\rho V_i (V_j n_j)$ on all bounding surfaces evaluates to the net force experienced by the body in the i^{th} direction. The former method, body-based perspective, is called the near-field method, while the latter method, flow-based perspective, is called the far-field method.

2.2.2 Bookkeeping methods applied to standalone nacelle

To study the aerodynamic forces on the standalone nacelle at cruise, a modified method that consists of a combination of near-field and far-field approaches is employed. The schematic of the nacelle surfaces and the captured inlet stream-tube are shown in fig. 2.2.

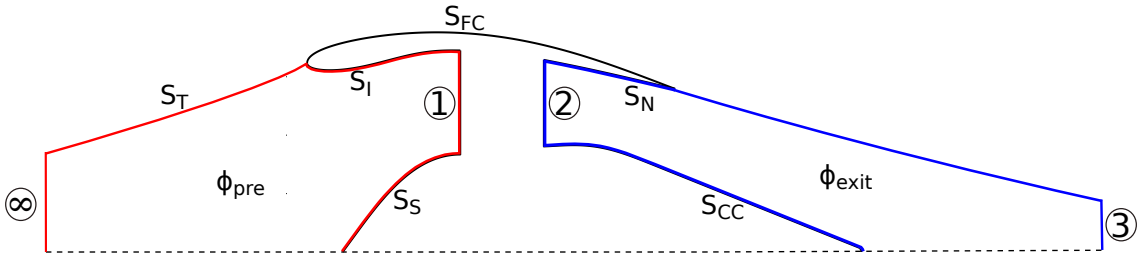

Figure 2.2: Description of nacelle surfaces and captured stream-tubes for estimating forces on nacelle.

A near field approach was used to evaluate the net propulsive force F_n. The net propulsive force sums up to the net forward force produced by the engine and the nacelle installation together.

$$F_n = -\int_{S_{skin} \cup S_1 \cup S_2} [\rho(u_x - u_\infty)(\mathbf{U}.\mathbf{n}) + (P - P_\infty)\mathbf{n}_x - (\tau_x.\mathbf{n})]\, dS \tag{2.17}$$

Aliter, Desterac's notations can be used to denote the integrand in the following way [20].

$$F_n = \int_{S_{skin} \cup S_1 \cup S_2} (\mathbf{f}.\mathbf{n})\, dS \tag{2.18}$$

where f is given by,

$$f = \rho(u_x - u_\infty)(\mathbf{U}.\mathbf{n}) + (P - P_\infty)\mathbf{n}_i - (\tau_x.\mathbf{n}) \tag{2.19}$$

The S_{skin} is comprises of all the nacelle surfaces except for the fan face plane and OGV exit plane. S_{skin} = $S_S \cup S_I \cup S_{FC} \cup S_N \cup S_{CC}$.

The net propulsive force is defined as the difference between the standard net thrust T_N and the inlet configuration drag D_c. The formulation of the standard net thrust is given by the following relation.

$$T_N = -\int_{S_N \cup S_{CC} \cup S_2} [\mathbf{f}.\mathbf{n}]\, dS + \int_{S_\infty} [\rho(u_x - u_\infty)(\mathbf{U}.\mathbf{n}) + (P - P_\infty)\mathbf{n}_x]\, dS \tag{2.20}$$

Subtracting the eqn. 2.17 from eqn. 2.20 yields the configuration drag D_c. The configuration drag is the summation of the pre entry drag ϕ_{pre} and the surface drag due to pressure and viscous effects on the fan cowling surface S_{FC}. Applying

linear momentum balance to the inlet capture stream tube, ϕ_{pre} can be estimated using the following balance equation.

$$\phi_{pre} = -\int_{S_I \cup S_S \cup S_1 \cup S_\infty} [\mathbf{f}.\mathbf{n}]\, dS \tag{2.21}$$

The total force on the fan cowling is accounted from both pressure and viscous forces in the following way.

$$\phi_{FC} = -\int_{S_{FC}} [(P - P_\infty)\mathbf{n}_x - (\tau_x.\mathbf{n})]\, dS \tag{2.22}$$

The configuration drag is the defined as the summation of ϕ_{pre} and ϕ_{FC}. The drag coefficient c_d is defined as follows.

$$c_d = \frac{D_c}{0.5\rho u_\infty^2 A_{ff}} \tag{2.23}$$

The drag force is normalized with the freestream axial velocity u_∞ and the fan face area A_{ff}.

2.3 Aerodynamic performance parameters

2.3.1 Intake performance parameters

The important intake performance parameters used in nacelle optimization studies and analysis are mass flow capture ratio (MFCR), intake pressure recovery η_i and the flow distortion parameter DC_{60}. The **mass flow capture ratio** (MFCR) relates to the extent of spillage in a nacelle intake. It is defined as the ratio of the inlet capture streamtube face area A_∞ to the nacelle highlight area A_{hi}.

$$MFCR = \frac{A_\infty}{A_{hi}} \tag{2.24}$$

MFCR is an important parameter during cruise operation as it heavily influences the pre entry force ϕ_{pre} and the pressure forces on the cowl $\phi_{c,p}$.

The **intake pressure recovery or** η_i indirectly dictates the fractional loss in the total pressure as the flow moves through the intake section. However, this parameter actually defines the fraction of total pressure that can be recovered as the flow moves through the intake. It is defined as the ratio of area-averaged total pressure at the fan face to the free stream total pressure.

$$\eta_i = \frac{\overline{P}_{t,ff}}{P_{t\infty}} \tag{2.25}$$

The DC_{60} presents a quantitative measure of the inlet flow distortion in the form of loss of local total pressure in a 60° sector defined on the fan face. The difference

in the area-averaged total pressure between the entire fan face and the considered sector is normalized with the dynamic pressure at the fan face q_{ff}.

$$DC_{60} = \frac{\overline{P}_{t,ff} - \overline{P}_{t,60}}{\overline{q}_{ff}} \tag{2.26}$$

Figure 2.3 shows the position of the annular section that is used to compute the DC_{60} parameter

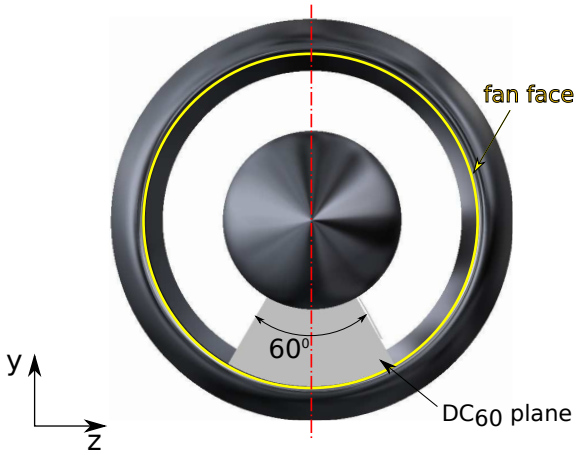

Figure 2.3: Schematic representation of the 60° sector plane used to calculate DC_{60} for TO condition.

The position of DC_{60} plane for the crosswind condition is defined in the results section.

2.3.2 Nozzle performance parameters

To quantify the nozzle performance for the optimization study, the following important nozzle performance parameters were defined. The **discharge coefficient** c_{dis} is an important parameter that determines how good a nozzle design is when compared to ideal conditions. c_{dis} accounts for the flow blockage effects and shear layer growth. It is defined as the ratio of the actual mass flow through the nozzle to the ideal nozzle mass flow.

$$c_{dis} = \frac{\dot{m}}{\dot{m}_{ideal}} \tag{2.27}$$

From isentropic realtions, the ideal mass flow is given by the following relation.

$$\dot{m}_{ideal} = AP_t \left(\frac{1}{\lambda}\right)^{\left(\frac{1}{\gamma}\right)} \sqrt{\frac{2\gamma}{(\gamma-1)RT_t}\left(1 - \left(\frac{1}{\lambda}\right)^{\frac{\gamma-1}{\gamma}}\right)} \tag{2.28}$$

The term λ in the equation 2.28 represents the nozzle pressure ratio. It is defined as follows.

$$\lambda = \begin{cases} P_{t2}/P_\infty, & \text{if } P_{t2}/P_\infty < PR_{crit} \\ PR_{crit}, & \text{if } P_{t2}/P_\infty > PR_{crit} \end{cases} \tag{2.29}$$

The definition of the critical pressure ratio is as follows.

$$PR_{crit} = \left(\frac{\gamma+1}{2}\right)^{\frac{\gamma}{\gamma-1}} \tag{2.30}$$

The critical pressure ratio determines if the nozzle is choked or not. Ideally, a choked nozzle has a Mach number of 1 at its throat.

Likewise, the **thrust coefficient** c_{th}, another important nozzle performance parameter, is defined as the ratio of the actual gross thrust produced by the nozzle flow to the product of nozzle mass and the ideal nozzle velocity. The c_{th} accounts for the thrust losses due to shear layers, non-isentropic flow effects like wall shear, shock effects, etc. The ideal nozzle velocity is given by the following relation:

$$V_{ideal} = \sqrt{\frac{2\gamma RT_t}{(\gamma-1)}\left(1-\left(\frac{1}{P_t/P_\infty}\right)^{\frac{\gamma-1}{\gamma}}\right)} \tag{2.31}$$

The definition of c_{th} is as follows.

$$c_{th} = \frac{T_g}{\dot{m}V_{ideal}} \tag{2.32}$$

The gross thrust T_g is estimated by integrating the forces on the nozzle surfaces and on the fan outlet guide vane (OGV) exit plane.

2.4 Governing equations for the flow field

For the compressible flow, the unsteady Favre averaged equations for mass and momentum transport equations are denoted as equation 2.33 and 2.34 respectively. Reynold's averaged variables are denoted with the superscript $(\bar{.})$ and variables subjected to density weighted (Favre averaging) are termed denoted with the $(\tilde{.})$ superscript.

$$\frac{\partial\bar{\rho}}{\partial t} + \frac{\partial}{\partial x_i}(\bar{\rho}\tilde{u}_i) = 0 \tag{2.33}$$

$$\frac{\partial\bar{\rho}\tilde{u}_i}{\partial t} + \frac{\partial\bar{\rho}\tilde{u}_i\tilde{u}_j}{\partial x_j} = -\frac{\partial p}{\partial x_i} + \frac{\partial}{\partial x_j}\left(\bar{\tau}_{ji} - \overline{\rho u_i'' u_j''}\right) \tag{2.34}$$

$$\frac{\partial}{\partial t}(\bar{\rho}E) + \frac{\partial}{\partial x_j}\left(\bar{u}_j(\bar{\rho}E+\bar{p})\right) = \frac{\partial}{\partial x_j}\left[-q_{l,j} - q_{t,j} + \overline{\tau_{ji}u_i''} - \frac{1}{2}\overline{\rho u_j'' u_i'' u_i''}\right] + \frac{\partial}{\partial x_j}\left[\bar{u}_i\left(\bar{\tau}_{ij} - \overline{\rho u_i'' u_j''}\right)\right] \tag{2.35}$$

Equation 2.4 is the energy balance equation in the differential form.

$$E = e + \frac{1}{2}\tilde{u}_i\tilde{u}_i + k \tag{2.36}$$

Here, e represents the specific internal energy and k is the turbulent kinetic energy, defined as $0.5(\widetilde{u_i''u_i''})$. Looking into the equation 2.34, the fluid stress tensor is dissociated into two parts, the mean stress tensor $\overline{\tau_{ji}}$ and the turbulent stress tensor $\overline{\rho u_i'' u_j''}$. The mean stress tensor, after using the constitutive relation looks as follows.

$$\bar{\tau}_{ij} = \mu\left[\left(\frac{\partial\tilde{u}_i}{\partial x_j} + \frac{\partial\tilde{u}_j}{\partial x_i}\right) - \frac{2}{3}\delta_{ij}\frac{\partial\tilde{u}_k}{\partial x_k}\right] \tag{2.37}$$

The turbulent stress tensor that results upon Reynolds decomposition is termed as τ_{ji}^R. Boussinesq's hypothesis is used to model this term to close the model. The modeled turbulent eddy viscosity μ_t is deduced from the turbulence parameters.

$$\tau_{ij}^R = \mu_t\left(\frac{\partial\tilde{u}_i}{\partial x_j} + \frac{\partial\tilde{u}_j}{\partial x_i}\right) - \frac{2}{3}\left(\bar{\rho}k + \mu_t\frac{\partial\tilde{u}_k}{\partial x_k}\right)\delta_{ij} \tag{2.38}$$

The laminar and turbulent heat flux vectors in the eqation 2.4 are defined as follows. Here, laminar and turbulent prandtl numbers are used respectively. These terms defines the diffusive transport of E by means of fluid and turbulent parameters.

$$q_{l,j} = -\frac{\mu c_p}{Pr_l}\frac{\partial\tilde{T}}{\partial x_j} \tag{2.39}$$

$$q_{t,j} = -\frac{\mu_t c_p}{Pt_t}\frac{\partial\tilde{T}}{\partial x_j} \tag{2.40}$$

Reynolds averaging done to equation 2.4 resulted in a turbulent diffusion term which can be modeled in the following way.

$$\overline{\tau_{ji}u_i''} - \frac{1}{2}\overline{\rho u_j'' u_i'' u_i''} = \left(\mu + \frac{\mu_t}{\sigma_k}\right)\frac{\partial k}{\partial x_j} \tag{2.41}$$

The first term on the left hand side corresponds to the molecular transport due to turbulent fluctuations and the other term corresponds to the diffusive transport due to turbulence.

For solving the turbulence parameters field, k-ω shear stress transport (SST) model by Menter [21] was employed. The SST model exploits the favorable features from both k-ϵ and k-ω turbulence models. The former one is more apt for freestream flows and the latter one works well close to the wall boundaries. The transport equations for the turbulent kinetic energy (k) and the specific dissipation rate (ω) are shown as follows.

$$\frac{\partial}{\partial t}(\bar{\rho}k) + \frac{\partial}{\partial x_j}\left(\bar{\rho}k\tilde{u}_j\right) = \tau_{ij}^R\frac{\partial\tilde{u}_i}{\partial x_j} - \bar{\rho}\beta^*\omega k + \frac{\partial}{\partial x_j}\left[\left(\mu + \frac{\mu_t}{\sigma_k}\right)\frac{\partial k}{\partial x_j}\right] \tag{2.42}$$

$$\frac{\partial}{\partial t}(\bar{\rho}\omega) + \frac{\partial}{\partial x_j}(\bar{\rho}\omega\tilde{u}_j) = \frac{\alpha}{\nu_t}\tau_{ij}^R\frac{\partial \tilde{u}_i}{\partial x_j} - \bar{\rho}\beta\omega^2 + \frac{\partial}{\partial x_j}\left[\left(\mu + \frac{\mu_t}{\sigma_\omega}\right)\frac{\partial \omega}{\partial x_j}\right] + D_w \quad (2.43)$$

Here, D_w is a cross-diffusion term that stems due to the fact that blending of k-ϵ and k-ω models is employed.

$$D_w = 2(1 - F_1)\bar{\rho}\frac{1}{\omega\sigma_{\omega,2}}\frac{\partial k}{\partial x_j}\frac{\partial \omega}{\partial x_j} \quad (2.44)$$

Blending functions F_1 and F_2 are used to switch from the k-ϵ model to k-ω model in the near-wall region. A linear interpolation function is used to interpolate field variables between the models. κ_1 and κ_2 are any field variables from the k-ω and k-ϵ model respectively. The interpolation function based on the wall distance is done as follows.

$$\kappa = F_1\kappa_1 + (1 - F_1)\kappa_2 \quad (2.45)$$

The model constants and the formulation of the turbulent Prandtl numbers for the transport of k and ω, σ_k and σ_ω are elaborately described in the FLUENT theory manual [22]. The following relation is used to evaluate the turbulent visocity μ_t.

$$\mu_t = \frac{\rho k}{\omega}\frac{1}{max\left[\frac{1}{a^*}, \frac{SF_2}{a_1\omega}\right]} \quad (2.46)$$

The fluid properties are modeled with ideal gas formulation. The fluid viscosity is approximated using a eighth-order polynomial with Sutherland's law.

2.5 Fan inlet coupling model

From a numerical perspective, modelling of the fan face boundary condition is challenging as it needs to account for the incoming flow distortions, i. e. local losses in total pressure and temperature, and setting the right static pressure profile on the pressure-outlet boundary. The fan-inlet coupling refers to the response of the fan face boundary condition to the distortion effects induced in the flow as a result of passing through the nacelle intake by doing more work in the regions where the total pressure loss is maximum. In the event of using a pressure outlet boundary condition, these effects aren't accounted for, as a constant average static pressure is applied throughout the entire boundary. It will be seen in the results that, although a constant pressure boundary condition worked well for the 2-D axisymmetric case, as seen from the good concurrence from the engine operation data, the calculation of pressure profile mitigates the over-prediction of flow separation effects in take-off and crosswind operating conditions for 3-D simulations.

A classical method, the parallel compressor theory, was used to model compression systems that experience distorted flows at inlet face [23, 24]. This method introduced the concept of dividing the compressor inlet face into two sectors, that refers to parallel compressors where, although there exists a difference in total pressure on the sector inlet faces, the compressors discharge at a constant back pressure. It can be theorized that the flow sector that ingests distorted flow possess low total pressure as a result of loss in flow energy due to flow re-circulation and turbulence. Hence, this compressor must work at a higher pressure ratio to match the same exit static pressure. It was also assumed that individual flow sectors had no cross-flow effects starting from inlet to discharge. The schematic of how the distorted flow can be captured with a sector is shown in fig. 2.4. This enables to better visualize how the theory of splitting the intake zone into two sectors accounts for inlet flow distortion effects.

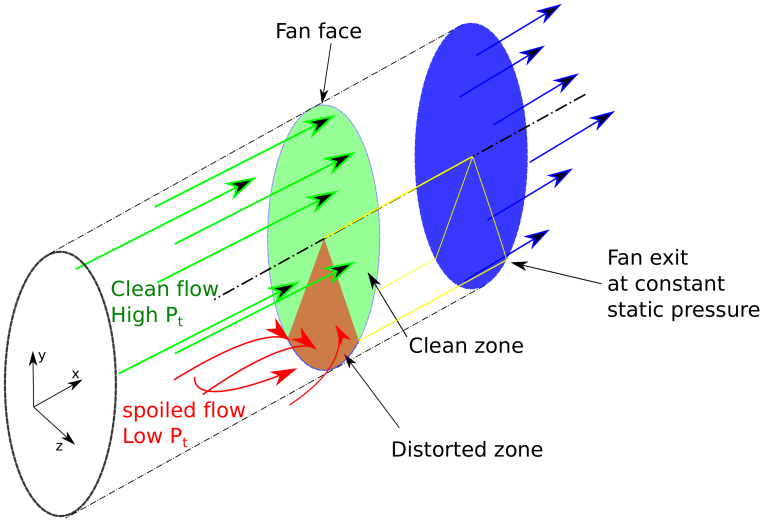

Figure 2.4: Schematic of the sector division done for parallel compressor method.

Adapting this classical to CFD analysis, a validated method called the modified parallel compressor (MPC) method was used to model the fan face boundary [25]. The implementation of MPC method is described as follows. The method described is shown for a single computational element denoted with superscript 'i' on the fan face. The same routine is carried out for the remaining elements on the fan face as well.

- The flow properties u_x^i, u_y^i, u_z^i, $\dot{m}$, P_1^i and T_1^i were obtained from the fan face for the current iteration along with the element face area A_1^i.
- The Mach number and stagnation properties M_1^i, P_{t1}^i and T_{t1}^i were deduced from the following isentropic flow relations.

$$M_1^i = \frac{V_1^i}{\sqrt{\gamma R T_1^i}} \tag{2.47}$$

$$P_{t1}^i = P_1^i \left(1 + \frac{\gamma - 1}{2} M_1^2\right)^{\frac{\gamma}{\gamma - 1}} \tag{2.48}$$

$$T_{t1}^{i} = T_{1}^{i}\left(1 + \frac{\gamma - 1}{2} M_{1}^{2}\right) \tag{2.49}$$

- The corrected mass flux ϕ from the obtained mass flow and stagnation properties were deduced using the following relation

$$\phi_i = \frac{\dot{m}\sqrt{(T_{t1}^{i}/T_{\text{inf}})}}{A_{1}^{i}(P_{t1}^{i}/P_{\text{inf}})} \tag{2.50}$$

- Based on the operating condition, fan performance curves based on corrected mass flux were used to find the fan Pressure ratio PR_i and isentropic efficiency η_i. The fan curves were linearized about the design operating point to enhance convergence and have better numerical stability.
- An imaginary plane having constant static pressure is defined downstream and the corresponding stagnation properties on that plane were deduced with reference to the current element using isentropic relations.

$$P_{t2}^{i} = P_{t1}^{i} * PR_i \tag{2.51}$$

$$T_{t2}^{i} = T_{t1}^{i}\left(1 + \frac{1}{\eta_i}\left(PR_{i}^{\frac{\gamma-1}{\gamma}} - 1\right)\right) \tag{2.52}$$

- The Mach number M_2^i and the static pressure P_2^i at the imaginary plane are evaluated from the Q-function and by inverting the equation 2.48.
- The OGV plane area A_2 and fan face area A_1 is used to determine the corresponding element area A_2^i assuming a constant area reduction factor A_{ratio}.
- A target static pressure $P_{2,targ}$ was defined based on the engine performance data. The pressure increment ΔP_i to be augmented to the inlet static pressure P_1^i is evaluated by the relation $\Delta P_i = \lambda(P_2^i - P_{2,targ})$. Here, λ is a weighing facor.
- These steps are iterated until the exit static pressure equals the target static pressure.

This method ensures that the local flow distortion effects are accounted in the fan face and the mass flow through the engine is altered as a result of the incoming flow properties.

3

Methods

3.1 Aerodynamic shape generation methods

This section describes the conventional and newly developed parametric design methods used to generate aerodynamic profiles. An illustration of how a parametric curve generation method can be applied to aerodynamic profile generation is also described in the upcoming sections.

3.1.1 Discrete or point cloud approach

The generation of aerodynamic profiles based on point cloud approach is highly constrained and requires a lot of discrete data [26]. This method requires a large volume of points with specific cartesian coordinates to define the curves properly near the nose and trailing edge regions of the aerodynamic profile. Moreover, the point cloud approach is a non-parameterized method which makes the design modification process laborious. It is also called the discrete method as the curves are defined by distinct points and it is unfeasible when considered to be used for shape optimization problems due to reduced control. Later, for aerodynamic applications, NACA profiles were developed, which were based on polynomials.

3.1.2 Polynomials and B-splines

The most commonly used parametric functions for curve generation are Splines and Bezier curves. Spline curves are based on piece-wise polynomials and are used widely in data applications. Compared to polynomial functions, splines possess better interpolation characteristics. In general, the formulation of Bezier curves is comparable to that of polynomial functions. With increased order of the polynomial, the round-off error relating to the control point is higher. So, a combinational fit of Bezier curves of low degree is preferred, usually termed as B-splines.

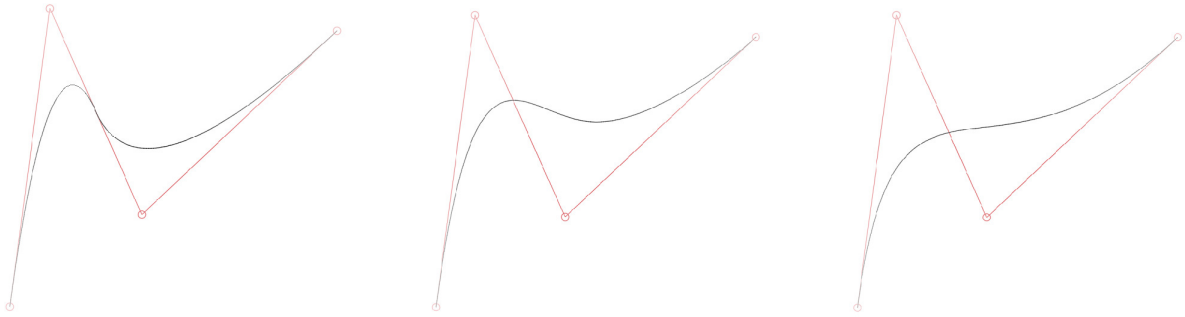

(a) Polynomial degree 2 (b) Polynomial degree 3 (c) Polynomial degree 6

Figure 3.1: Comparison of Non-Uniform rational basis spline (B-spline) fit to control vertices with varying curve degree.

Figures 3.1a-c show the fitness of the curve based on same control vertices and confirms that lower degree curves gives good fit and has low round-off errors. B-splines are advantageous over discrete methods as they require minimal control points.

3.1.3 Class-Shape Transformation (CST) method

The class-shape transformation (CST) is a robust and mathematically well-behaved curve generation methodology that was initially focused on satisfying shaping parameters of a subsonic airfoil with a view to reducing form drag and fine tuning the design parameters for good performance [26]. For instance, the ability of an airfoil to maintain attached flow depends on its nose radius (R_{LE}) and the aft body angle (β_{aft}) determines the aft-body separation characteristics. Additionally, CST methods enable the user to easily control the curve profiles since only a few optimization parameters are required. The lateral coordinate of the airfoil as a function of axial coordinate is described as follows:

$$\frac{z}{c} = S\left(\frac{x}{c}\right)\sqrt{\frac{x}{c}}\left[1-\frac{x}{c}\right] + \frac{x}{c}\frac{\Delta z}{c} \tag{3.1}$$

Here, the coordinates are non-dimensionalized with the chord length of the airfoil c. In the CST method, the curve generation is formulated by the product of a class function and a shape function. A brief description of these functions are described as follows:

Class Function : The class function defines the basic topology of the aerodynamic shape or the class of geometry, whether it has a blunt edge, pointed edge for the nose and trailing edge or a biconvex shape. Equation 3.1 shows a class function of the form $\sqrt{\frac{x}{c}}\left[1-\frac{x}{c}\right]$. In general, the class function as a function of $\frac{x}{c}$ is defined by the following relation.

$$C\left(\frac{x}{c}\right) = \left[\frac{x}{c}\right]^{N1}\left[1-\frac{x}{c}\right]^{N2} \tag{3.2}$$

Comparing with eqn. 3.1, it can be seen that for airfoils with blunt nose and sharp trailing edge, N1 and N2 must be set to 0.5 and 1 respectively. Figure 3.2 shows the various class functions that can be obtained from varying the exponents N1 and N2.

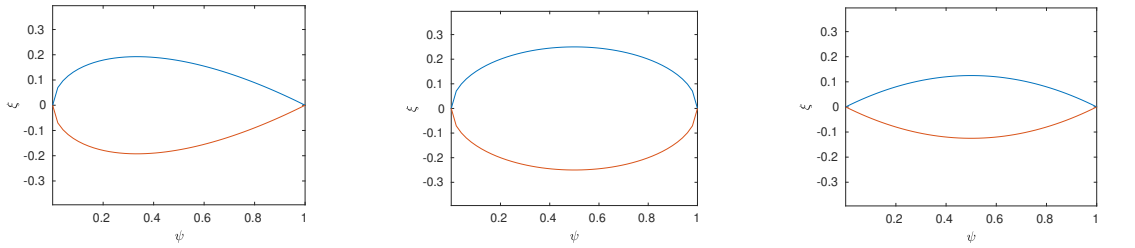

(a) NACA shape for airfoil N1 = 0.5 and N2 = 1

(b) Elliptical shape for airfoil N1 = 0.5 and N2 = 0.5

(c) Biconvex shape for airfoil N1 = 1 and N2 = 1

Figure 3.2: Class functions depiction based on variation in parameters N1 and N2

In Fig.3.2a, a general depiction of a NACA airfoil is obtained when N1 and N2 are set to 0.5 and 1 respectively, since a round nose is only possible with $\sqrt{\frac{x}{c}}$ term. This representation can be used for a NACA profile generator by superimposing the shape function which can modify localized characteristics of the profile.

Shape function: In equation 3.1, the term $S\left(\frac{x}{c}\right)$ is called the shape function. The shape function is a well behaved analytical function which contains information about the shaping characteristics that needs to be superimposed on the class function curve. For the considered airfoil geometry, the parameters that can be modified by the shape function are as follows:

- The nose leading edge radius (R_{LE})
- trailing boat-tail angle (β_{aft})
- The maximum thickness of the airfoil
- The axial position of the maximum thickness of the airfoil

The unitized airfoil geometry's leading edge nose radius and the boat tail angle and the airfoil trailing edge thickness are related to the shape function terms S(0) and S(1) respectively, in the following manner:

$$S(0) = \sqrt{2\frac{R_{LE}}{c}} \qquad S(1) = tan\beta + \frac{\Delta Z_{TE}}{c} \tag{3.3}$$

In fact, a series of varying airfoils can be generated by decomposing the shape function into algebraic sum of two functions like $S_n\left(\frac{x}{c}\right) = S_{1n}\left(\frac{x}{c}\right) + S_{2n}\left(\frac{x}{c}\right)$. Where, S_{1n} and S_{2n} are the decomposed shape functions. Further, composite unit airfoils can be generated by using a scaling factor that modifies the relative axial position of the maximum thickness. Using Bernstein polynomials as shape functions can be advantageous as they are mathematically well defined curves and the set of n+1 curves for a n^{th} order Bernstein functions add to one. This is called partition of unity. The depiction of the Bernstein polynomial of order n is formulated in

the following form.

$$BP_n(x/c) = \sum_{i=0}^{n} bp_i K_{i,n} x^i (1-x)^{n-i} \qquad K_{i,n} = \frac{n!}{i!(n-i)!} \tag{3.4}$$

Alterations to the shape function are brought by weighing the function with the bp_i term as shown in Equation 3.6. In Fig. 3.3, the effect of weighing terms on Bernstein curves considering 3^{rd} and 5^{th} order polynomial is depicted.

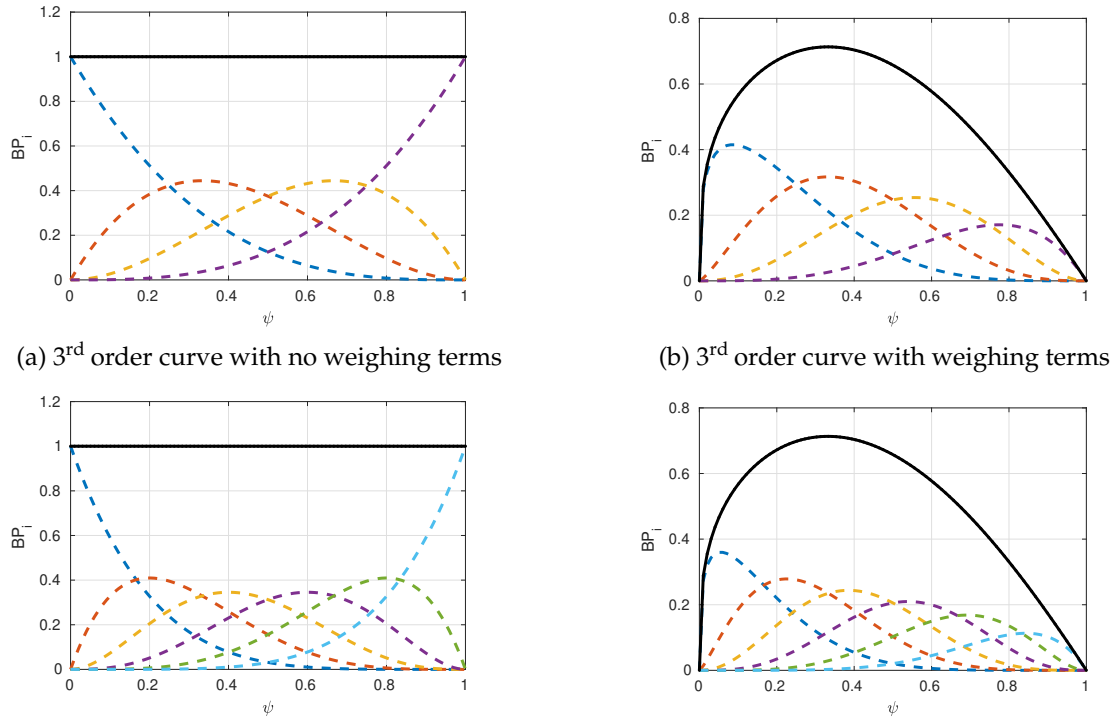

(a) 3rd order curve with no weighing terms

(b) 3rd order curve with weighing terms

(c) 5th order curve with no weighing terms

(d) 5th order curve with weighing terms

Figure 3.3: Depiction of $3^{rd}$and 5^{th} order Bernstein polynomial curves

In a typical parametric study involving aerodynamic profiles, the set of weights are solved based on the constraints that need to be satisfied by forming a system of linear equations of the for **A.X = B**. Adapting to the non-dimensionalized abscissa and ordinate by $\psi = x/c$ and $\xi = z/c$, the shape function based on bernstein polynomials can be represented in the following way:

$$S(x/c) = \sum_{i=0}^{n} bp_i K_{i,n} \psi^i (1-\psi)^{n-i} \tag{3.5}$$

The final representation of the ordinate ξ^k as a function of ψ is depicted in the following equation:

$$\xi^{(k)}(\psi) = \left[\sum_{i=0}^{n} bp_i K_{i,n} \psi^i (1-\psi)^{n-i} C(\psi) \;+\; \psi \Delta\xi_{te} \right]^{(k)} \tag{3.6}$$

To parameterize a curve with a sharp trailing edge and blunted leading edge using the CST method, the constraints including position, maximum radius, extents, gradients, etc. need to be non-dimensionalized with a design reference length like the chord. The first and last Bernstein polynomials are deduced from the leading edge radius and trailing edge angle and offset as shown in Eq. 3.3, while the set of remaining Bernstein polynomials to be solved are depicted as follows:

$$X = \begin{bmatrix} bp_1 & bp_2 & ..... & bp_{n-1} \end{bmatrix}^T \tag{3.7}$$

$$B = \begin{bmatrix} b_{1,0} & b_{2,0} & ..... & b_{n-1,0} \end{bmatrix}^T \tag{3.8}$$

$$A = \begin{bmatrix} a_{1,1} & a_{1,2} & ..... & a_{1,n-1} \\ : & : & : & : \\ : & : & : & : \\ a_{n-1,1} & a_{n-1,2} & ..... & a_{n-1,n-1} \end{bmatrix} \tag{3.9}$$

Matrix A depicted in Eq. 3.9, is the transformation matrix that solves for the set of Bernstein weighing polynomial vector X in Eq. 3.7. The entities present in the transformation matrix and constant matrix B are deduced from the formulation and derivatives of the shape function. This set of analytical linear set of equations passes through the positional constraints and also satisfies the gradients. A detailed comparative study was done between the actual and parameterized shape of a nacelle outer cowl and intake portions with a low order approximation method and the geometric variations were found to be less than 0.6% based upon the local curvature of the profile [27].

From the literature, it can be seen that the CST method provides a good fit for an initial aerodynamic profile when designed even with limited design constraints [27]. Further performance analysis done on the CST aerodynamic profile, considering intake performance such as IPR and inlet distortion parameters, shows a good fit to the actual aerodynamic profile. CST curves have been extensively used for designing nacelles and nozzles for aero-engines [references]. The method has shown to be able to design nacelles with good aerodynamic performance characteristics such as low total pressure losses and distortion, good drag rise characteristics, etc..

Figure 3.4 shows an illustration of how the physical constraints can be imposed on a CST model of the nacelle cowling. The class function used in the cowling parameterization corresponds to a blunt leading edge and a sharp trailing edge with N1 and N2 set to 0.5 and 1 respectively.

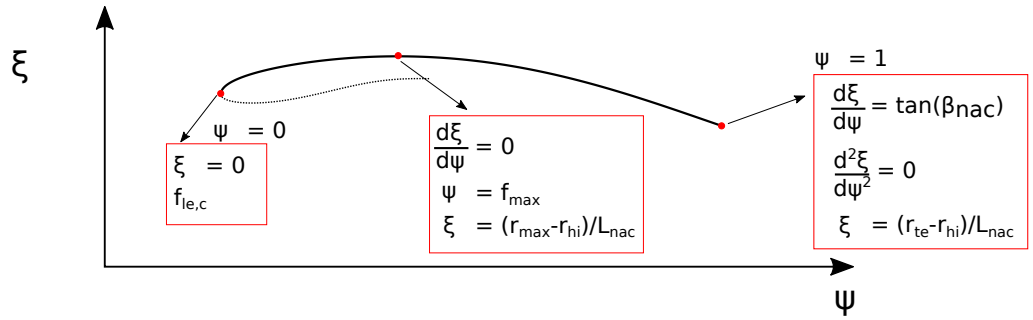

Figure 3.4: Schematic representation of setting constraints to the nacelle cowl geometry

For the cowl parameterization, the chord length was normalized to unity in ψ scale and the radial coordinates were normalized using r_{hi} and L_{nac}, represented using ξ. A 3^{rd} order CST polynomial was used for the parmaterization. At the trailing edge corresponding to $\psi = 1$, the curve gradient, the radial coordinate and the curvature were explicitly specified. The curve gradient $\frac{d\xi}{d\psi}$ is embedded in the last Bernstein polynomial bp_n and need not be accounted separately. However, the second derivative $\frac{d^2\xi}{d\psi^2}$ influences the polynomial coefficients. The maximum radius position on the curve is specified as a positional constraint with explicit ξ and ψ values. Unlike the case with the trailing edge condition, the $\frac{d\xi}{d\psi} = 0$ criteria influences the Bernstein polynomials. At the leading edge, the positional constraint for ψ doesn't influence the Bernstein polynomial that needs to solved while the non-dimensionalized leading edge radius was defined in the Bernstein polynomial bp_0.

3.2 Parametric nacelle design procedure

3.2.1 Nacelle design method

Over the years, consistent advancements have been seen in aerodynamic shape optimization techniques and drag estimation methods. This trend is driven by the necessity to develop high BPR turbofan engines for commercial airliners, and thus led to the introduction of well posed shaping methods like the CST methods for nacelle profiles. Further, intuitive CST or iCST techniques resulted in better aerodynamic performance owing to enhanced curve smoothness [27]. Generally, nacelle drag reduction is crucial as it allows for better fuel efficiency, enabling a reduction in emissions, noise reduction, and structural support [28].

Essentially, the multi-point aerodynamic design of the nacelle considered in the present study starts off with a 2D axisymmetric design for cruise operation. Further, the obtained design was subjected to profile modifications at specific circumferential positions so that these modifications benefit aerodynamic performance at other operating points like take-off and crosswind. The overall nacelle design consists of an asymmetric outer cowling and intake and a symmetric nozzle. An

intuitive approach is used to formulate the design space parameters, considering inputs from the literature. However, a trial-and-error-based approach was used to finalize the design limits of several parameters so as to avoid nonphysical geometries. The parameterization and optimization variables for the nacelle and nozzle profiles are presented in the subsequent sections.

3.2.2 Spinner design selection and criteria

In the preliminary nacelle design phase, a super-ellipse-shape based spinner profile was employed. Due to practical concerns regarding ice accretion over the spinner surface, it was decided to employ a sharp-tipped spinner to mitigate ice accretion. From an experimental standpoint, it was observed that the ice accretion was quite predominant on the conical spinner, 60%-80% more compared to the elliptical and coniptical shapes [29]. A coniptical spinner has a pointed leading edge, representing the apex of a cone, and an elliptical rear part. For the present study, a CST curve was employed in the rear part, instead of an elliptical profile. Figure 3.5 shows the different spinner designs with varying half-cone angles (HCA).

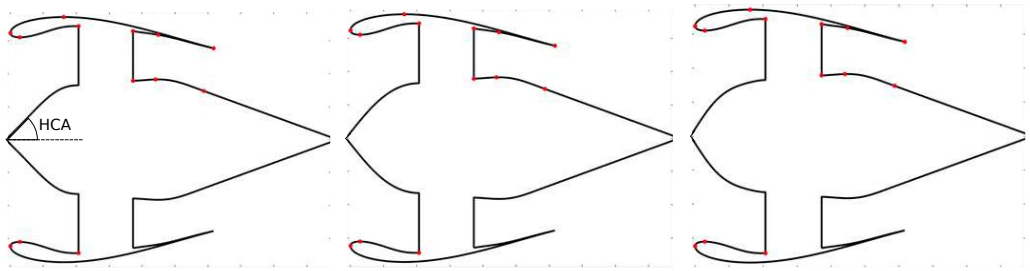

a) HCA 45^0 b) HCA 51^0 c) HCA 57^0

Figure 3.5: Spinner comparison based on Half cone angle (HCA)

Based on 2-D axisymmetric analysis, the design with the least HCA had the maximum c_d and minimum IPR. The spinner design with a HCA of 51° was chosen for further research due to its balance between ice-accretion and reduced c_d. However, only cruise operation was investigated for the initial design, where only a minimal difference in the output parameters was observed. An off-design study for other operation conditions would have resulted in a different result, but it was beyond the scope of the study.

3.2.3 Nozzle profile parameterization

The important nozzle design parameters and their definitions are discussed in this section. The nozzle parameterization was divided into the nozzle, outer cowl profile, core cowl, and aft-body curves as shown in Fig. 3.6. The design of nozzles considers a multitude of performance aspects, such as reducing c_d during cruise operation and generating the desired level of thrust during take-off. Further, the

nozzle design impacts the exhaust jet performance, and hence an optimized design is deemed to ensure that the fan operates at a desirable operation point [30]. The nozzle outlet area determines the operating point for the fan at cruise and take-off. It's a trade between high efficiency at cruise and high stability at take-off.

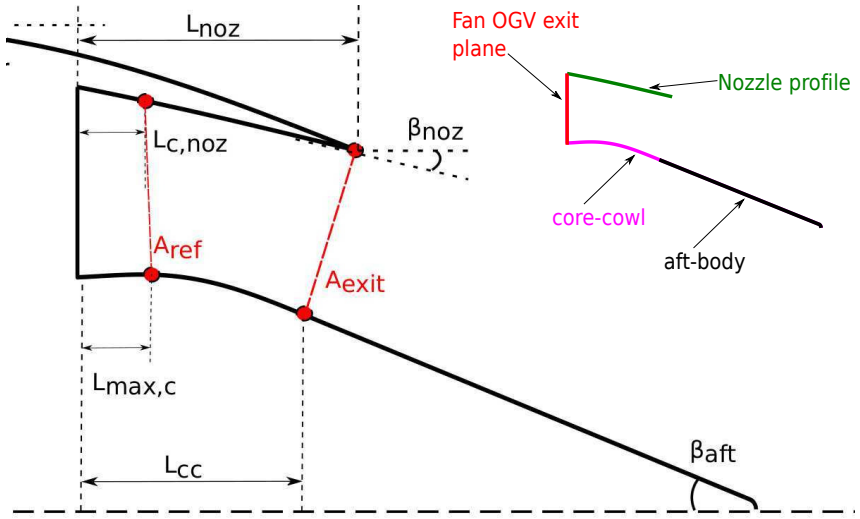

Figure 3.6: Geometric data needed for nozzle parameterization

The considered nacelle optimization parameters are shown in table 3.1. The range of the considered optimization parameters was defined based on the initial nozzle design. Of the considered parameters, β_{aft} geometrically modifies the total length of the aft-body and thus needs to be chosen based on geometric constraints.

Table 3.1: Nozzle and core profile optimization parameters.

Parameter	Formulation	Range
Nozzle angle	β_{noz}	12-14 [°]
Aft-body angle	β_{aft}	18-24 [°]
Axial position of max. radius on core cowl	$f_{max,cc} = L_{max,c}/L_{cc}$	0.28-0.36
Axial position of nozzle control point	$f_{noz} = \frac{L_{c,noz}L_{cc}}{L_{noz}L_{max,c}}$	0.85-1.15
Nozzle Area ratio	$AR_{noz} = A_{ref}/A_{exit}$	1.185-1.212

The parameter f_{noz} was defined relative to $f_{max,c}$, a parameter that defines the axial position of the maximum radius on the core cowling. This design parameter extensively influences the nozzle profile and ultimately influences the thrust coefficient c_{th} and the nozzle discharge coefficient c_{dis}. The formulation of these nozzle performance parameters was described in the sub-section 2.3.2.

3.2.4 Nacelle profile parameterization

The schematic representation of the nacelle design parameters is depicted in Fig. 3.7. The same figure shows the two adjoining profiles, viz., the outer cowling or cowl profile and the intake profile. The intake profile impacts the flow ingestion characteristics at various operating points. The lip design has a great impact on the flow separation characteristics, while the cowling design influences the spillage effects.

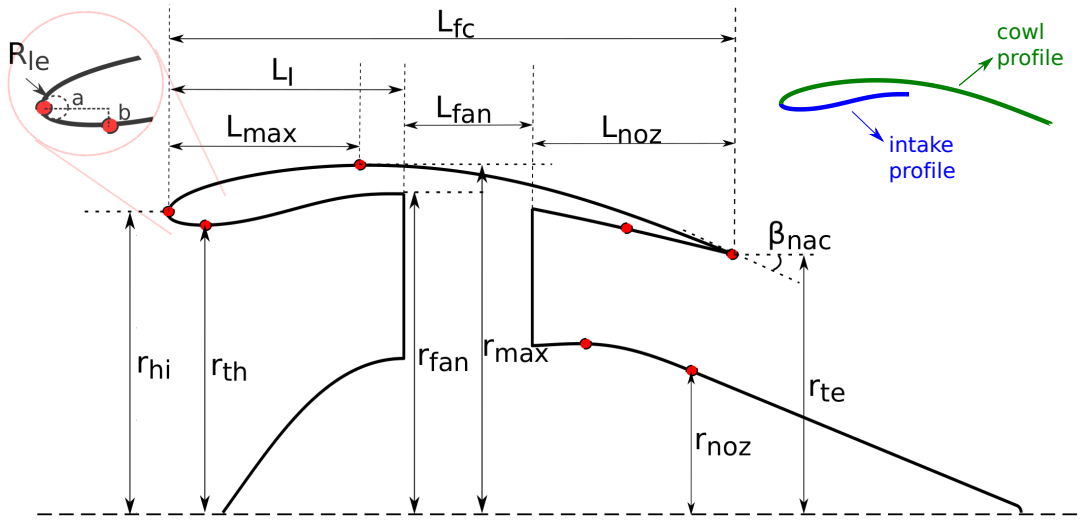

Figure 3.7: Geometric data needed for nacelle parameterization

The set of optimization parameters used for nacelle optimization are shown in table 3.2. Of these considered parameters, the contraction ratio (CR), lip aspect ratio (AR_{lip}) and the intake leading edge radius of curvature ($f_{le,I}$) are the parameters that relate to intake profile shape.

Table 3.2: Nacelle outer cowl and inlet profile optimization parameters.

Parameter	Formulation	Range
Highlight radius normalized	r_{hi}/r_{fan}	0.8 - 0.86
Maximum radius normalized	r_{max}/r_{fan}	1.09 - 1.18
Axial position of maximum radius	$f_{max} = L_{max}/L_{fc}$	0.35 - 0.42
Cowl leading edge radius of curvature (non-dimensionalized)	$f_{le,c} = \frac{R_{le,c} f_{max} L_{fc}}{(r_{max}^2 - r_{hi}^2)}$	0.95 - 1.4
Nacelle boattail angle	β_{nac}	19 - 24
Intake leading edge radius of curvature (non-dimensionalized)	$f_{le,I} = \frac{R_{le,I} f_{th} L_I}{(r_{th}^2 - r_{hi}^2)}$	0.95 - 1.4
Contraction ratio	$CR = \frac{r_{hi}^2}{r_{th}^2}$	1.08 - 1.25
Lip aspect ratio	$AR_{lip} = a/b$	1.55 - 3.5

In take-off and crosswind operation conditions, it will be shown in the later sections that the intake profile shaping plays a major role in the mitigation of flow separation and corresponding flow distortion at the fan face.

3.2.5 Cowl geometry generation

For the 3-dimensional asymmetric nacelle generation, 3 parameterized 2-D shape profiles representing cowling and intake, namely crown, keel, and maximum half-breadth (MHB), are positioned circumferentially as shown in Fig. 3.8. Considering a cylindrical coordinate system that is axially coincident with the nacelle's centerline axis, the crown, keel, and MHB profiles are circumferentially positioned at azimuthal angles of $\Phi = 0°$, $\Phi = 90°$ and $\Phi = 180°$ respectively.

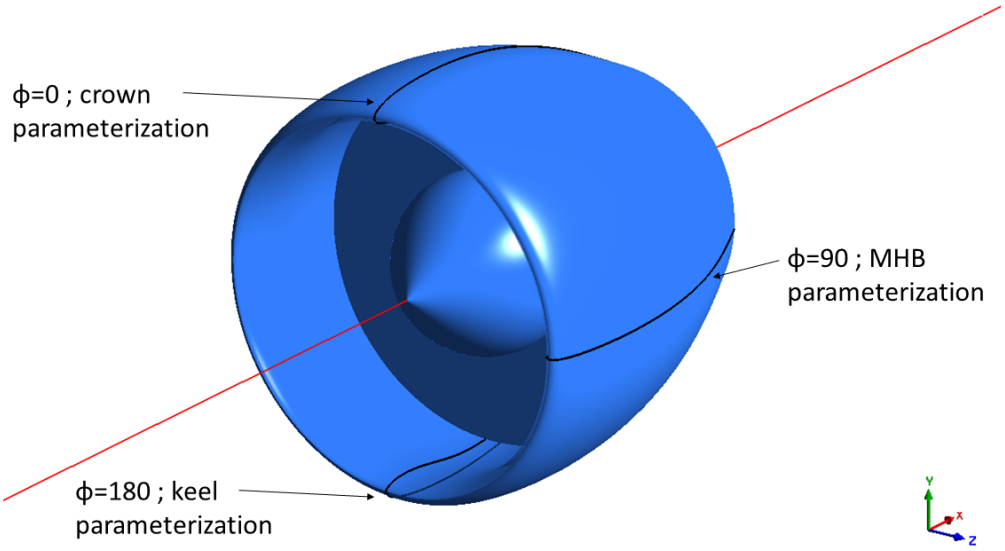

Figure 3.8: 3D represenation of the nacelle geometry

To obtain a smooth variation in profile in circumferential and radial directions, a sinusoidal interpolation was done circumferentially for the axial (x) and radial (r) coordinates. This ensures a continuous transition between the aforementioned profiles along axial and radial directions. The nacelle is designed to be symmetric about the mid-plane, which is co-planar with the keel and crown profiles. In other words, the nacelle geometry spanning circumferentially from $180° < \Phi < 360°$ is a mirror image of the geometry at $(0° < \Phi < 180°)$.

3.2.6 Drooping transformation of the inlet profile

Drooping of a nacelle is a geometric transformation technique that tilts the intake and cowl portion proportionately for better alignment with the incoming flow during cruise operation. Essentially, an under-wing installation causes a wing

upwash that introduces a deviation in flow direction with reference to the nacelle's geometric axis. Usually, a local angle of attack in the range of 3°-5° is seen for a wide range of turbofan engines.

Figure 3.9 shows a comparison of a drooped intake and cowling with a 2D axisymmetric base design. The centre of the fan face plane, denoted by point P, is the pivot point about which the drooping transformation is made. The drooping angle θ_d is the angle enclosed between the drooped inlet axis and the existing nacelle's centerline.

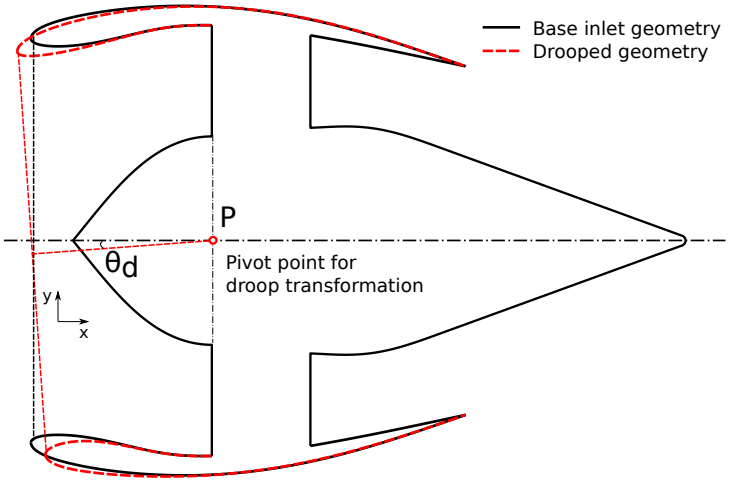

Figure 3.9: Schematic of nacelle inlet drooping

The initial inlet profiles were treated with a shape deformation function that transforms the original CST curves. The distinct function values for the crown and keel positions are deduced based on θ_d. The transformed coordinates for the cowl and intake in x and y directions are related to a second degree polynomial based on the distance from the point P. In other words, the extent of shape transformation is higher at locations axially away from point P, and maximum deformation is observed at the highlight positions (leading edge of the forebody). Drooped inlets in modern intakes allow for better flow alignment and thus reduced c_d during cruise operation [31].

3.3 Multipoint operation description

For the multi-point nacelle analysis, the following operating conditions were considered: cruise, take-off, and crosswind. A detailed description of each operating point is provided in this section.

3.3.1 Cruise operation

Considering a standard flight envelope, cruise operation takes up a major part of the entire flight operation. Hence, it is desired to have the lowest possible c_d for the cruise operation. This accounts for reduced fuel consumption and efficient nacelle aerodynamics. Figure 3.10 shows the schematic of cruise case setup.

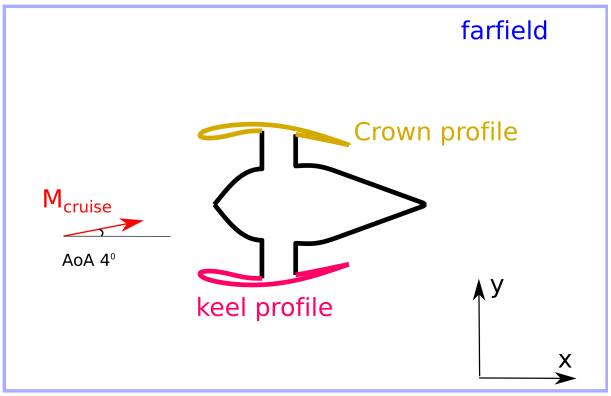

Figure 3.10: Schematic representation of cruise operating point.

The flight Mach number is the maximum for the cruise operation condition considering the entire flight profile. In the cruise condition considering no side wind, the crown and keel profile are the most investigated parts so as to avoid abrupt diversions in flow streamlines and to have good intake aerodynamic performance. These factors account for reduced configuration drag or its coefficient c_d.
The wing up-wash effects account for a local angle of attack in an under-wing engine installation that is slightly higher than the flight's geometric angle of attack, which remains within 2-3 ° [32]. in theory, a lift-generating wing (airfoil) has a velocity deficit on the pressure side owing to a short travel path relative to the suction side and in case of a real world scenario, deviations in the aforementioned theory can be seen owing to turbulence effects. This causes a difference in the flow streams around the airfoil, and this leads to a local velocity component upstream of the wing [33]. Here, the cruise AoA was taken to be 5° owing to the up-wash and flight AoA for better representation of the flow experienced by the nacelle. This local effect reduces the effective lift and introduces a new drag component called the induced drag [34]. To facilitate good flow alignment during cruise, inlet drooping of nacelles can be beneficial.

3.3.2 Take-off operation

The take-off condition is a critical operating point in the flight envelope where the nacelle experiences incoming flow at high AoA. In this operating condition, the engine produces enormous thrust to generate the necessary lift force to set the aircraft airborne and eventually climb to level flight. This condition majorly challenges the keel profile design, as at high AoAs, the lower part of the inlet is susceptible to experiencing flow separation at the lip and consequent high levels of flow distortion. Distorted flow can cause fan stall and a reduction in thrust

production. Figure 3.11 shows the case description for the take-off (TO) operating condition.

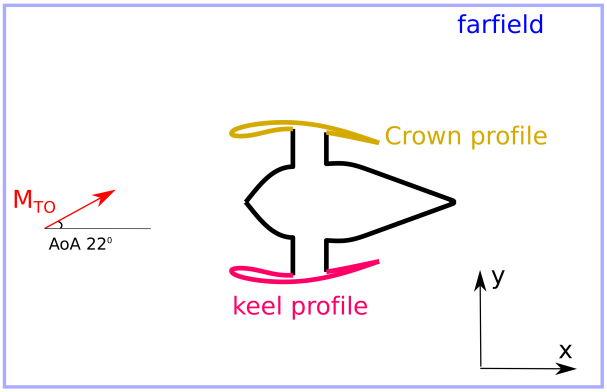

Figure 3.11: Schematic representation of take-off (TO) operating point.

The local AoA for the TO operation was considered to be be 22°. This value was evaluated considering the aircraft's geometric orientation and the local wing up-wash phenomenon. The geometric AoA found in the literature is in the range of $14° - 17°$ [35]. The aircraft AoA for the TO analysis was evaluated for the maximum lift from the literature and the local AoA was deduced considering an added wing up-wash effect. The maximum lift AoA was chosen as an extreme condition that would lead to a conservative nacelle design. However, in normal flight conditions, the nacelle will not be subjected to such a high AoA.

3.3.3 Crosswind operation

Unlike the previously considered cases, a modification to the classical pure cross-wind operation was made due to the unavailability of engine operation data and the corresponding fan performance curve. The modified description of the cross-wind case is explained in detail in the section 4.4.3.1.

3.4 Computational setup

To solve for the flow fields around the nacelle in the computational domain, a finite volume discretization approach was used. The discretized Reynolds Averaged Navier Stokes (RANS) equations were iteratively solved using a pressure-based solver to obtain a converged flow field.

3.4.1 Computational grid

The computational mesh used in the 3D simulations is a full multiblock structured mesh. The mesh generation was done with the commercial meshing software ANSYS ICEM CFD. The mesh for the selected design based on cruise analysis is shown in Fig. 3.12.

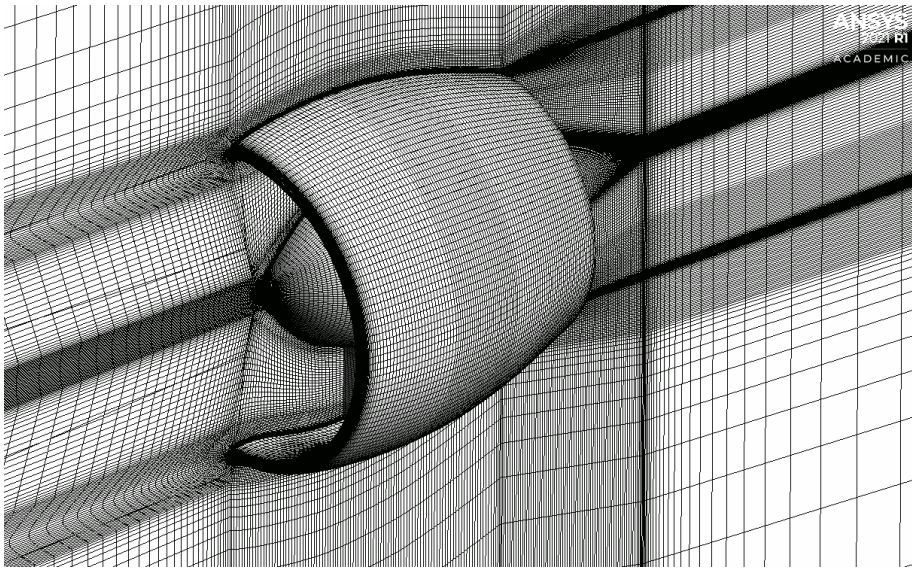

Figure 3.12: The 3D computational mesh used in the present analysis.

The mesh generation process was automated based on the topology of the nacelle geometry using a script. A MATLAB function is used to write a mesh script, specific to the ICEM mesher that controls the meshing and exporting options within the ICEM meshing software. First, the generated 3D surface profiles were converted to point clouds that can be loaded from the meshing software. The aforementioned script detects the named shape profiles and associates each with their respective blocks. The information of no. of divisions and element growth ratio for all blocks edges were predefined.

Comparative studies done on varying first element height along the wall normal direction showed no significant differences in estimation of configuration drag. The study resulted in a range of wall y^+ values from 1 to 30. However, in order to be consistent with the literature and as a general best practice, the first element height was chosen so that y^+ 1 was satisfied.

3.4.2 Boundary conditions

The description of the 2D computational domain and the boundary conditions employed are represented in Fig. 3.13. The 2D computational domain is used for the 2D axisymmetric nacelle analysis, meaning that the flow AoA = 0°. Symmetry (slip-walls), pressure inlet and pressure outlet boundary conditions were employed for the outer domain boundaries. The pressure inlet and pressure outlet boundaries in the outer domains were assigned with the estimated free stream pressure and temperature values from isentropic relations discussed in the section 2.1.

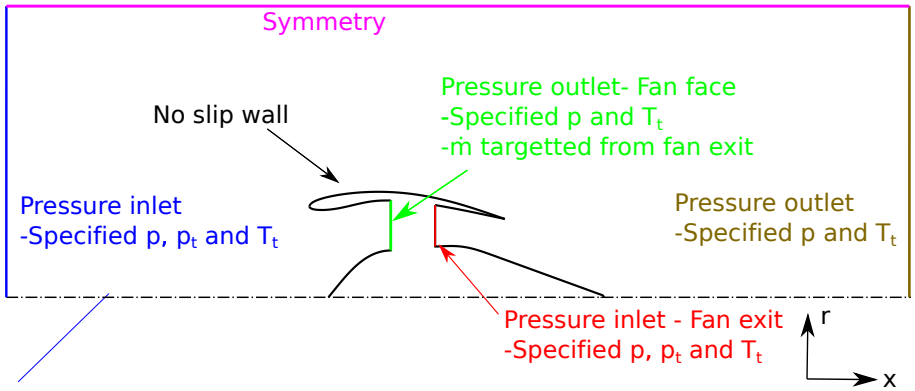

Figure 3.13: Schematic of the 2D computational domain and Boundary conditions.

Pressure inlet and pressure outlet boundary conditions were set to OGV exit face and fan face boundaries respectively. A constant pressure profile (uniform static pressure) was used for the fan face boundary. To maintain flow continuity throughout the engine for estimating accurate forces, $\dot{m}$ was trageted at fan face boundary from the OGV exit face. An adiabatic no-slip wall boundary condition was assigned to all surfaces. Owing to 0 swirl flow component, the spinner was assumed to be a fixed wall as opposed to being assigned a rotational component. The dashed lines represent the axis of symmetry in Fig. 3.13. The 3D computational domain is cylindrical and the lateral view of the domain is shown in Fig. 3.14.

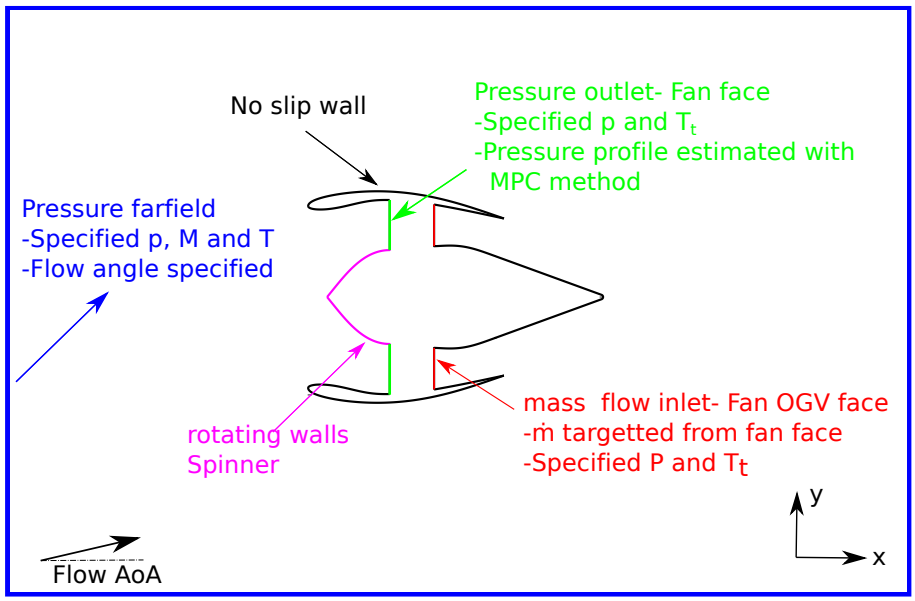

Figure 3.14: Schematic of the 3D computational domain and Boundary conditions.

The outer domains were assigned as pressure farfield boundary conditions as it can account for incoming flow at low and high AoAs. This is not possible with symmetry boundary condition being assigned to the lateral walls as it sets the

surface normal component of flow ($\vec{V}.\vec{n}$) to zero. Pressure outlet boundary condition was used at fan face with the modified parallel compressor (MPC) method that sets the pressure profile. Instead of targeting $\dot{m}$ at fan face, mass flow inlet boundary was set at the fan OGV exit face. This ensures that mass continuity through the thruster is satisfied for accurate evaluation of forces on boundaries and thrust. Adiabatic no slip walls were assigned to all nacelle surfaces. Rotational motion consistent with engine operation, about the x-axis was defined on the spinner walls. This ensures that the swirl introduced by the spinner is captured well in the computational domain.

3.5 Workflow for multi-objective optimization

The shape optimization problem used to optimize the nacelle and nozzle parameters was defined as a multi-objective optimization case. By a multi-objective optimization problem definition, it means that the solver explores the design space to find the Pareto-optimal evaluations that satisfy the two objective functions to a maximum extent. The design space consists of various evaluations that has a set of optimization variables. A brief description of how the optimization solver is used for the present optimization and how the optimization workflow was designed for the nacelle and nozzle optimization is provided in the following sections.

3.5.1 Solver description and optimization workflow

The optimizer used in the present study is a multiobjective evolutionary algorithm (EAs), non-dominated sorting genetic algorithm (NSGA-II). It was proven that the NSGA-II is essentially faster in nondominated sorting and has a reduced order of computational complexity compared to its predecessors, besides possessing good spread and enhanced convergence near the Pareto-optimal space [18]. The schematic of the optimization workflow is shown in Fig. 3.15. The functions used in the optimization workflow are described below:

- A **main GA function** controls the overall optimization workflow. The design variables pertaining to the initial population and the design space are specified in this function. The initial set of population was selected from a Latin hypercube sampling.
- The **objective function** receives/sends data from the NSGA-II function and also communicates with nacelle geometry generator to create the geometry, generate the mesh, conduct CFD analysis and store the data. Besides, design penalization criteria is also added to the objective function.
- In the **constraint** function, geometric and performance constraints were set based on the nacelle thickness at the various locations. However, design penalization method proved to be quite effective and resulted in more evaluations near the feasible zone.

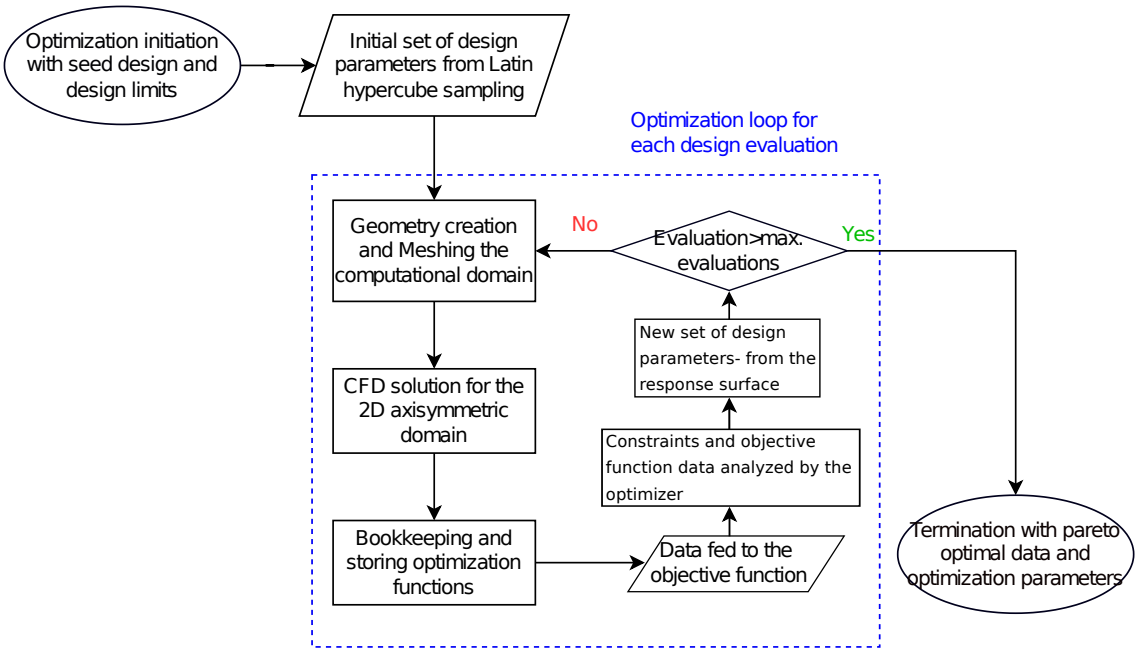

Figure 3.15: Flowchart describing the Optimization workflow.

3.5.2 Nozzle optimization method

For the nozzle optimization study, the optimization workflow mentioned in the aforementioned section was employed, except that an additional loop was used within the objective function to correct the nozzle exit area to match the $\dot{m}$ to the desired design mass flow rate $\dot{m}_{des}$. This internal loop ensures that $\dot{m}$ and PR_{fan} are kept constant and the engine operating point is fixed for each design evaluation.

3.5.2.1 Formulation of A_{noz}-$\dot{m}$ correction loop

Theoretically, the nozzle exit area A_{exit} bears direct proportionality with $\dot{m}$ when the nozzle inlet stagnation properties are fixed as per the following isentropic flow relation.

$$\frac{\dot{m}}{A} = \frac{P_t}{\sqrt{RT_t}} f\left(\gamma, M\right) \tag{3.10}$$

Since the total pressure at fan OGV station P_{t2} is fixed for the 2-D CFD simulations, The nozzle exit area A_{exit} was varied to match the engine design point mass flow rate. To facilitate this, an internal mass flow-area correction loop was added to the objective function to correct the mass flow and its operation is shown in Fig. 3.16. The final exit area correction was deduced through establishing a linear proportionality ratio between A_{exit} and corresponding $\dot{m}$ based on the first two iterations. The subsequent area correction iterations were brought about through linear extrapolation of the obtained data. The threshold for $\dot{m}$ was set to 0.1% with respect to the target design point mass flow. Typically, convergence was obtained within 2-3 iterations, while the maximum no. of iterations was set to 4.

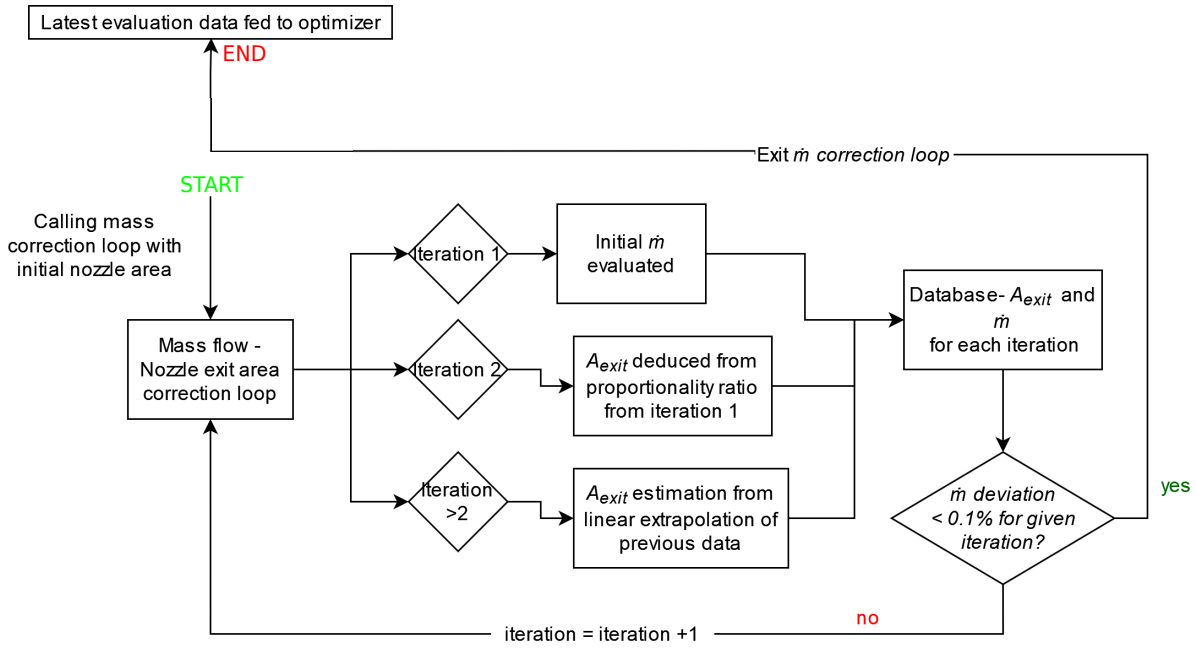

Figure 3.16: Schematic of internal mass flow- nozzle area correction loop.

3.5.2.2 Nozzle optimization specification

Constraints: Since an optimized nacelle profile from a base study was used for the nozzle optimization study, no thickness constraints were set as the optimized nacelle cowl satisfied all geometric constraints. For the same reason, constraints on IPR proved to be redundant as the intake geometry was same throughout the study. So, no constraints were used.

Design penalization: Penalization for design with low IPR, i.e, IPR < 0.998 were set. This snippet scales the objective functions by a factor of 10 and positions it away from the feasible design space. Thus, the learns to look into a different set of variables within the feasible zone.

Design space: The optimization variables and the associated design limits are mentioned in table 3.1. The optimization run had 10 generations with a population size of 10 individuals.

3.5.3 Nacelle optimization method

For the nacelle optimization study, the optimized nozzle geometry as it had better c_{th} and c_{dis}. The optimization was done for 2025 evaluations where the no. of generations was 45 and the population size was 45 as well.

Design penalization: Since nacelle cowling optimization was involved in this study, design penalization was done on two parameters.

- Cowling thickness constraints were defined at various axial locations in the cowl.
- Designs that possess IPR less than 0.998 were penalized as well.

If any of the aforementioned criteria were to be overruled, the concerned evaluation was penalized by scaling up the objective functions so that it is moved to unfeasible design space.

Design objectives: The objective of the optimization is to design a nacelle with a low c_d and A_{wetted}. Thus, these two parameters were selected as objectives. The design selection was based on giving more priority to designs with the least c_d.

Design space: The optimization variables and the corresponding design space was populated in table 3.2.

4

Results and discussions

The results and findings are structured in a chronological order in the results section. Starting with 2-D multi-objective design optimization studies for the nozzle and nacelle geometries, a best nozzle geometry was chosen based on nozzle optimization parameters. Subsequently, a nacelle optimization study was done with the fixed nozzle and the good designs are chosen based on the outputs from the optimizer. These designs were subject to 3D asymmetric analysis and further design modifications. For the 3D asymmetric analysis,

- The axisymmetric design was tested for cruise operation and the positive effect of inlet drooping was quantitatively assessed.
- The best design from cruise operation was tested for an intense climb operation condition. The effect of inlet drooping and profile modifications at keel were investigated.
- Finally, the obtained design was subjected to further profile modifications at MHB and crown positions to avoid flow separation at crosswind operation.

4.1 Mesh Independence study

A mesh convergence study was carried out to determine the sensitivity of the converged solution field to changes in the number of cells in a computational domain. For the 2-D and 3-D simulations, a global mesh refinement factor was used to uniformly change the element count in all the directions in the structured mesh blocks, which facilitates uniform scaling of the mesh model without altering the mesh topology. An initial study on the wall y^+ values pointed to an appreciable variation in the results when wall functions were employed. As a consequence, to be consistent with the literature, the thickness of the first element was explicitly specified in the mesh module to satisfy $y^+ < 1$ [22]. The results from the mesh convergence studies, where the variations in the design parameters are evaluated based on the finest mesh, are presented in the figs. 4.1 and 4.2 for the 3-D and 2-D computational domains, respectively. For the 3-D mesh validation study, the drag coefficient c_d and the normalized net propulsive force F_{net} were studied for variations. The mesh size was varied from 3.26 x 10^6 to 15.07 x 10^6 for the coarsest and finest mesh models, respectively.

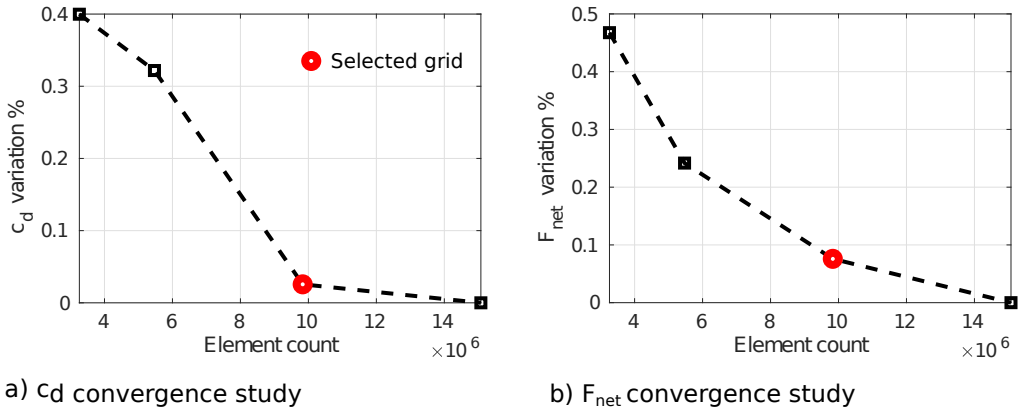

a) c_d convergence study b) F_{net} convergence study

Figure 4.1: Mesh independency study on chosen parameters for the 3-D computational domain.

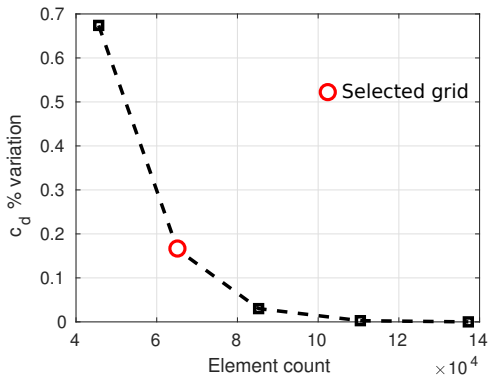

Figure 4.2: Mesh independency study on c_d for the 2-D computational domain.

In the 3-D mesh validation study, relative to the finest grid, the chosen mesh model varies in c_d and F_{net} by 0.026% and 0.076% respectively. The grid corresponding to a maximum variation in c_d of 0.2% was chosen for the 2-D mesh validation study because a fine grid will necessitate extensive computational resources for the design optimization studies.

4.2 Multi-objective shape optimization of nozzle and core-cowl

The initial optimization studies done on the shape parameterization of the nacelle also included the nozzle parameters as optimization variables. Out of the considered 11 total optimization variables, 3 variables described the nozzle geometry. The findings indicated that changes in nozzle properties, particularly the geometric parameters β_{aft}, β_{noz}, and $f_{max,cc}$, had a significant impact on engine mass flow, nozzle pressure ratio, thrust coefficient, c_{th}, and discharge coefficient, c_{dis}. These effects weren't desirable as every parameter set that represented a nacelle and nozzle profile together had different engine operation points. Hence,

it is deemed to maintain a constant engine operating point for all evaluations in the design space. The fan pressure ratio PR_{fan} was maintained constant owing to a fixed total pressure at the OGV plane and a constant intake design with a constraint on IPR.

The results from the optimization study for the five nozzle parameters described in the section 3.2.3, considering discharge coefficient c_{dis} and thrust coefficient c_{th} as optimization functions are shown in fig. 4.3a. The study was carried out with a fixed nacelle design that was obtained from a previous optimization study and had good intake performance. At least 100 design evaluations were necessary to get good design convergence and an established pareto front. To verify that the engine operates at the design point, the variation in performance parameters was studied. Figure 4.4 shows mean variation in engine power, F_{net}, $\dot{m}$ and PR_{fan} are less than 0.1%.

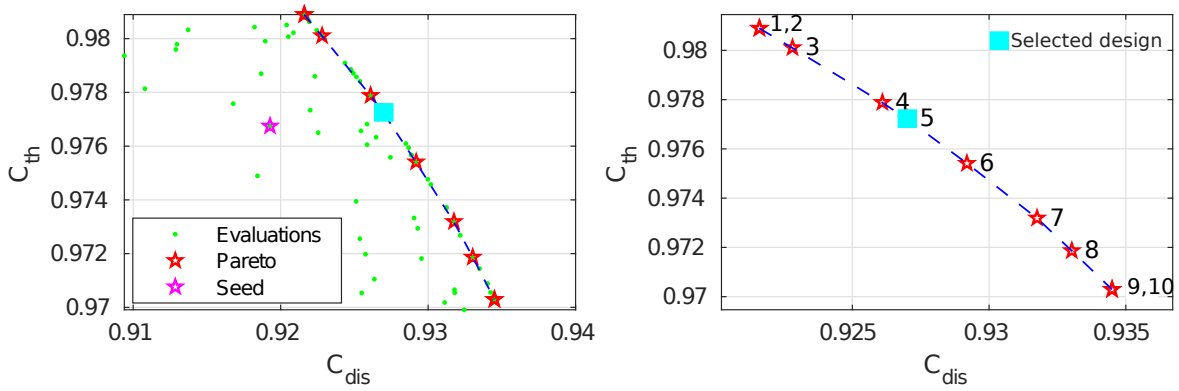

Figure 4.3: Population and Pareto-front plots from the multi-objective nozzle optimization study.

The selected design 5 had an aft angle β_{aft} which was very close to the seed design. This was done to ensure that the aft body length does not vary between the seed (baseline) design and the optimized design. Apart from variations in c_{th} and c_{dis}, c_d and F_{net} do not vary expressively among all the good evaluations on the pareto front.

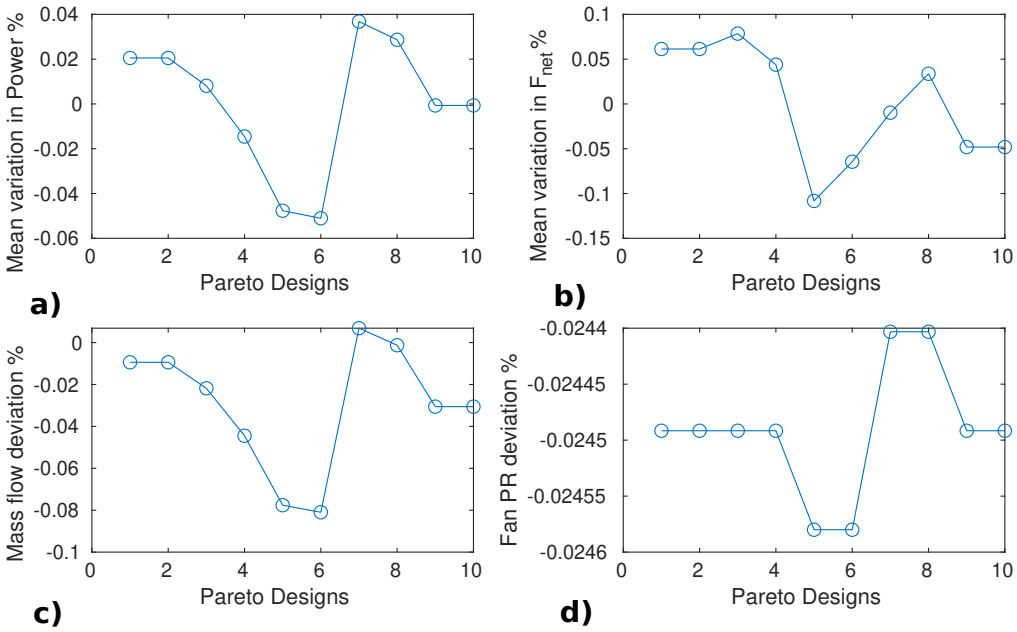

Figure 4.4: Performance parameters of the Pareto-optimal evaluations from nozzle optimization study.

4.3 Multi-objective shape optimization of a axisymmetric nacelle

Two of the main parameters associated with nacelle performance are the drag coefficient c_d and the wetted area A_{wetted}, as discussed in the section 3.2.4. The configuration drag, or its coefficient c_d accounts for the pre-entry forces ϕ_{pre}, intake force at the fan face, and cowl shear forces. It has been assumed that designs which possess low wetted area also possess low enclosed cowl volume, hence are lighter. So the optimization problem was formulated to look for feasible designs that maintain a balance between c_d and A_{wetted}. The fixed nozzle geometry from the previous study is used to ensure that the engine operates very close to the design point on the performance map. Although minor differences were obtained in the results, consistent nacelle performance parameters were obtained with fixed nozzle geometry. Figures 4.5 and 4.6 show the multi-objective design space and performance metrics of all evaluations.

Figure 4.5 shows the feasible evaluations and the obtained pareto-optimal designs. Here, the punished evaluations are not shown. It is evident from the design space shown in fig. 4.6a-d that the search for the good designs was confined to two distinct zones that have different intake designs and intake momentum drag budget. In other words, the GA receives the same c_d as an optimization input for two distinct designs that has contrasting geometric features, especially the parameter r_{hi}/r_{fan}. This hindered the optimizer from exploring the complete design space as understood from the performance metric comparisons shown in

fig. 4.6.

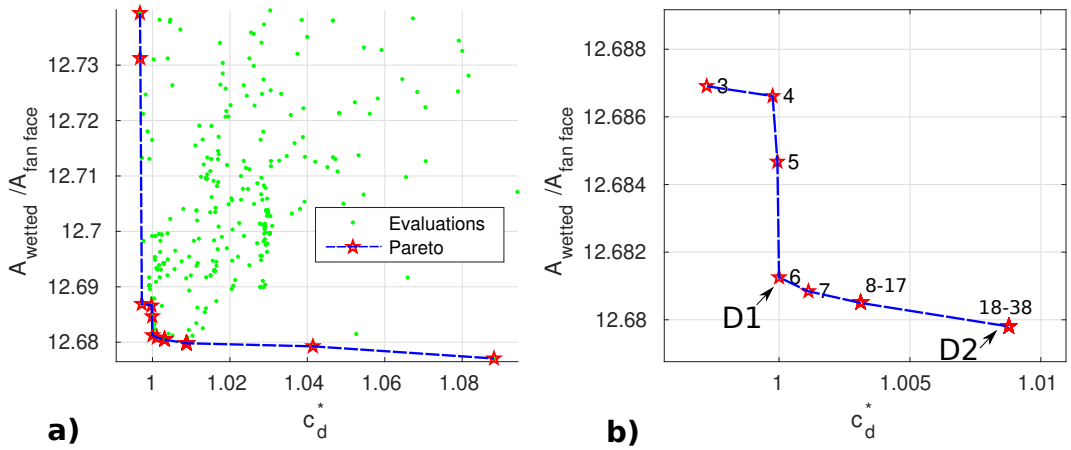

Figure 4.5: Population and Pareto-front plots of feasible evaluations from the multi-objective nacelle optimization study.

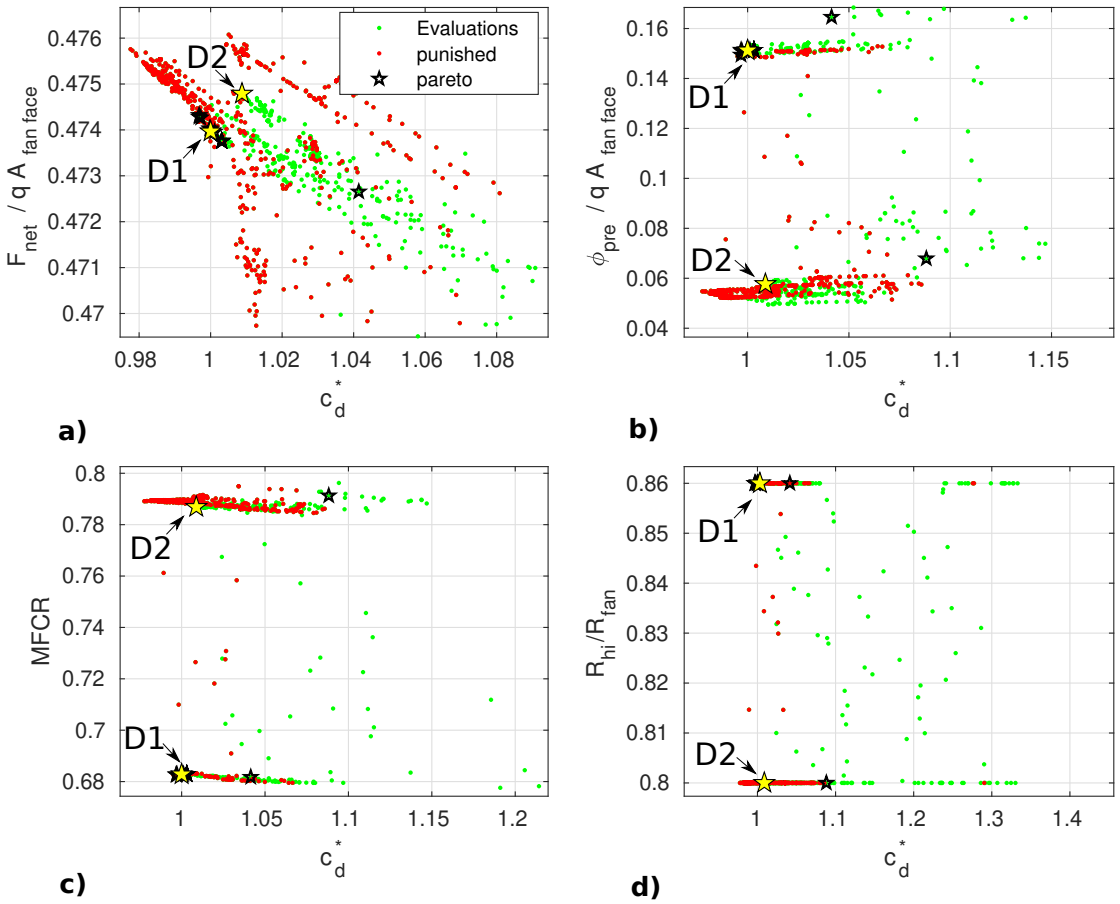

Figure 4.6: Performance metrics and geometric parameter of all evaluations. (c_d normalized based on design D1)

It was observed that the parameter r_{hi}/r_{fan} either goes to the lower bound or the upper bound confining the search to two distinct zones, each possessing different MFCR. So, A trial and error based approach was used to set the design space for the nacelle parameters over various studies. The design space for the optimization study shown in this section has been adjusted so that the obtained designs had a MFCR ranging from 0.67 to 0.8.

4.3.1 Detailed comparison of high-spillage and low-spillage designs

Two good designs, D1 and D2, possessing the least A_{wetted} were selected from the pareto front shown in the figure 4.5. These designs were selected from either design zones bearing contrasting intake parameters, as seen from the positions of the designs in the performance and geometry comparison shown in the fig. 4.6. The designs D1 and D2 can be treated as high and low spillage intakes, respectively. Higher flow spillage occurs in the design D1 owing to the low MFCR. This also suggests that design D1 is more susceptible to flow acceleration as the flow is less aligned with the mean camber line and the streamlines have to turn around the lip more aggressively. The normalized drag budget and intake performance parameters are compared in Table 4.1.

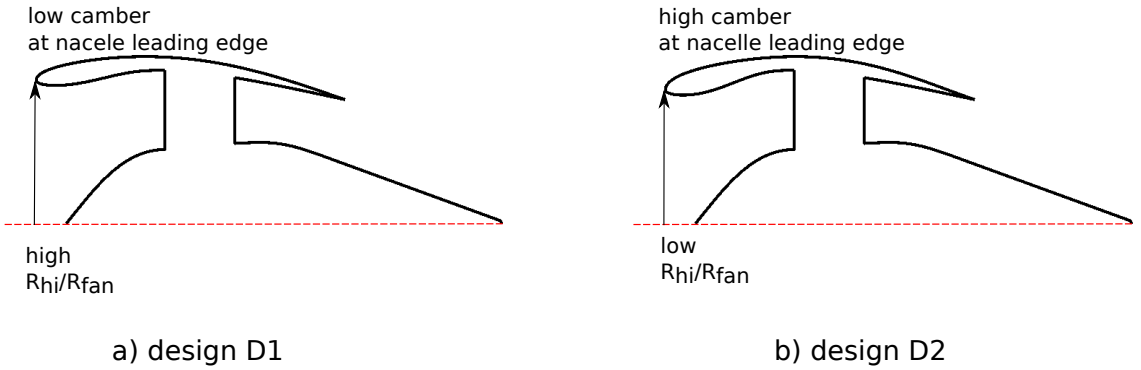

Figure 4.7: Design Schematics comparing designs D1 and D2.

Table 4.1: Comparison of Drag budget and normalized intake forces $(Forces/qA_{ff})$ for designs D1 and D2.

Designs	c_d^*	ϕ_{pre}/qA_{ff}	$\phi_{c,v}/qA_{ff}$	$\phi_{c,p}/qA_{ff}$	MFCR	η_i
D1 (High-spillage)	1	0.1513	0.01781	-0.0923	0.6829	0.9995
D2 (Low spillage)	1.0088	0.05767	0.01801	0.0016	0.7869	0.9992

c_d^* normalized based on D1

Comparing the normalized ϕ_{pre} between the designs D1 and D2, as expected, large pre-entry force was obtained for design D1. The low MFCR seen in design

D1 casts a large annular area S_T, besides high pressure and reduced dlow velocities at the entry station in the intake-capture stream tube as seen in fig. 2.2. This leads to high pre-entry force. However, a negative cowl pressure force $\phi_{c,p}$ was seen in D1 owing to the lip suction effect. Although, the viscous forces on the cowl $\phi_{c,v}$ is quite similar for both the designs, the pressure component of drag $\phi_{c,p}$ for D1 being negative, balances out the high ϕ_{pre}. On the other hand, for design D2, $\phi_{c,p}$ is comparatively larger in magnitude. But, it sums up to similar value of configuration drag as D1 since ϕ_{pre} for D2 is lower.

The pressure coefficient c_p profiles from 2-D axisymmetric studies were shown in fig. 4.8. For the ease of visualization, the normalized cowl and inlet profiles are shown in fig.4.8b to understand the location of c_p plot. A similar visualization for c_p plots is intended to be used in the following sections as well.

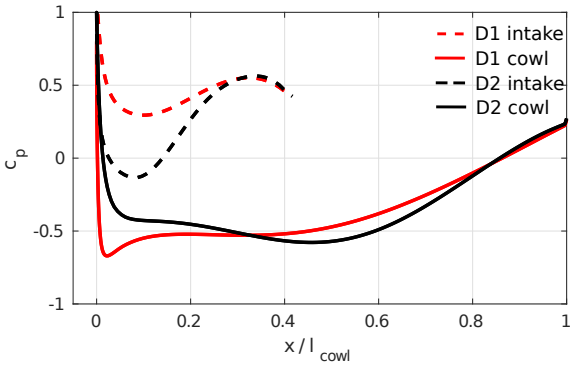

a) Distribution of Pressure coefficeint on Intake and cowl

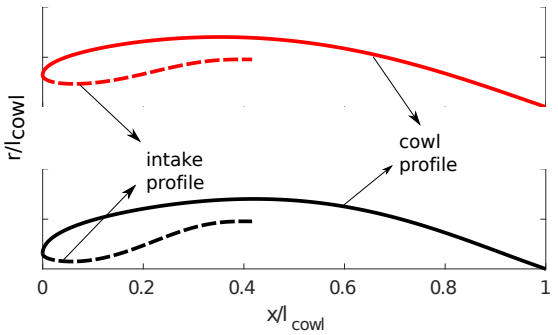

b) Cowl and intake profile normalized with cowl length l_{cowl}

Figure 4.8: Pressure coefficient profiles and aerodynamic profiles of intake and cowl for designs D1 and D2.

Figure 4.8a shows a steep reduction in pressure for design D2 at the intake profile, as seen by the reduction in c_p. This is due to the reduction in throat area compared to D1. In the case of the flow approaching at an AoA, this trend may increase the susceptibility of flow separation at intake near the keel profile. On the contrary, only a modest drop in pressure was seen for D1, which matches with the Mach number contours showing a relatively weaker acceleration bubble on the intake side for D1 as seen from fig. 4.9. Owing to increased incidence between the geometry and the incoming flow in the high spillage design D1, a steep drop in c_p is observed for design D1 on the cowl as seen in fig.4.8a. This is seen as an acceleration bubble on the cowl in Mach number contours.

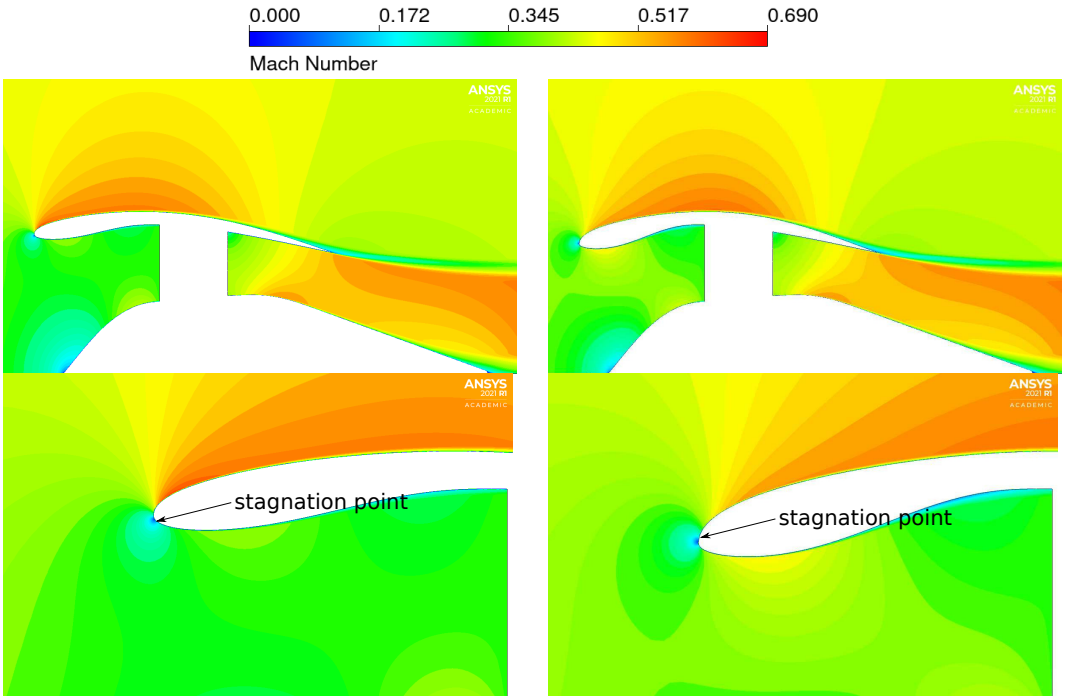

a) Design D1 b) Design D2

Figure 4.9: Mach number contours for designs D1 and D2 from 2-D axisymmetric simulations.

The analogy of cambered airfoils can be used to visualize the effect of flow acceleration over the suction side considering the position of the stagnation point. For cambered airfoils, in general, the stagnation point moves towards the suction side with an increase in camber angle. Because of the low camber angle of the airfoil, the streamline curvature is higher, which is visible as an acceleration bubble on the suction side. Since the excess static pressure on the cowl with respect to P_∞ is normalized with free-stream dynamic pressure ($P_{t\infty}$-P_∞), the position where c_p equals 1 in fig. 4.8 is the flow stagnation point on the surface. Although the stagnation points in designs D1 and D2 were positioned axially at different locations, the c_p plots make this difficult to see due to the 0 AoA.

4.4 3-D computational analysis

A 2-D axisymmetric analysis done in the previous sections, compared and contrasted the highlighting flow features between designs D1 and D2. In the following section, a similar comparison was done on designs D1 and D2 with a 3-D computational domain. Owing to wing up-wash effects from the under wing installation of the nacelle, the flow AoA for the cruise condition is set to 4°. For all 3-D analysis, c_d^* values were deduced with respect to design D1b, a derivative of design D1.

4.4.1 Cruise operation condition

The different cases studied in axisymmetric and asymmetric cruise operation point are tabulated below. For the cruise operation analysis, With the flow AoA set to 4°, extensive comparisons were done for varying droop angle θ_d.

Table 4.2: Designs studied for 3-D asymmetric analysis

DESIGNS			
$\theta_d[^\circ]$	**D1**	**D2**	AoA [°]
0 (axisymmetric)	D1a	-	0
0 (axisymmetric)	D1b	D2b	4
2	D1c	-	4
4	D1d	-	4

4.4.1.1 Axisymmetric design analysis- Comparing D1b and D2b

The results from axisymmetric 3-D cruise analysis showed similar flow trends as of 2-D axisymmetric case discussed in section 4.3.1. The figures 4.10 and 4.11 show the Mach number contours and the surface pressure plots (c_p) respectively.

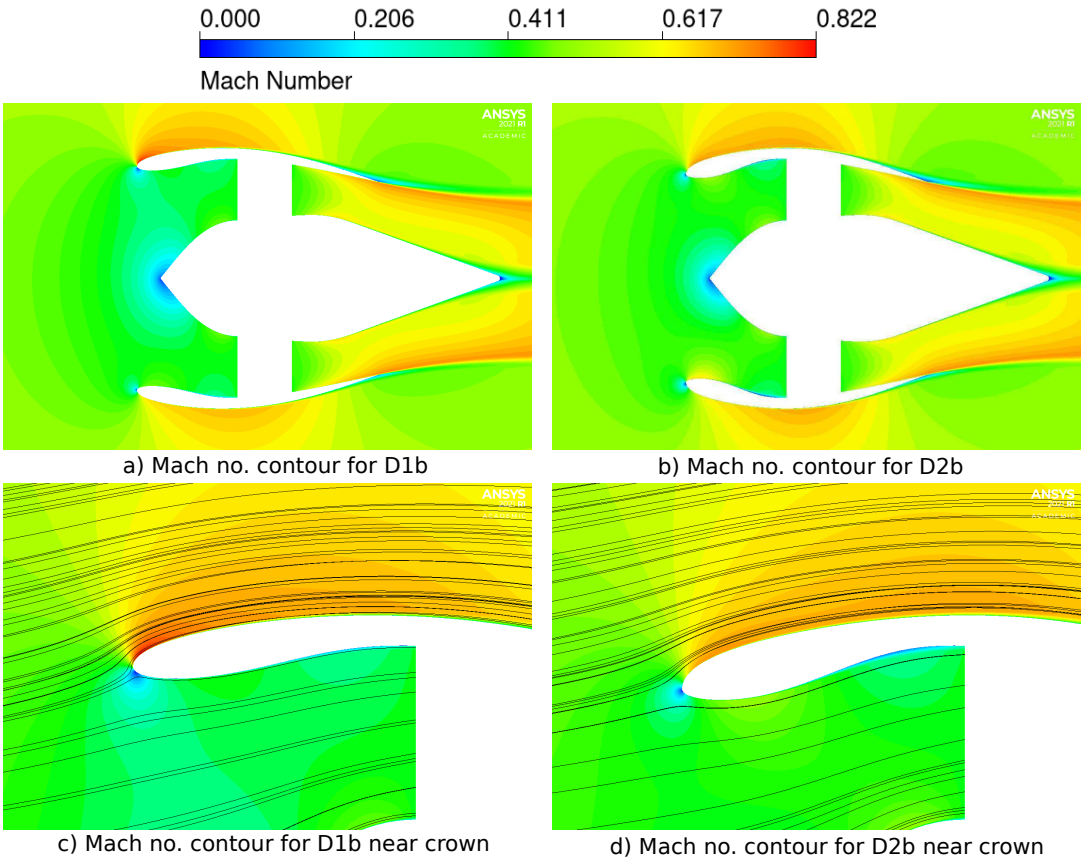

Figure 4.10: Mach no. contour comparison for designs D1b and D2b for cruise at 4° AoA.

Owing to a non-zero AoA, as expected, an acceleration bubble was present over the cowl for design D1b as seen in fig.4.10c. On the contrary, in the Mach no. field for the design D2b shown in fig. 4.10b, a small acceleration bubble was seen on the intake profile at keel, which is followed by a low momentum flow zone.

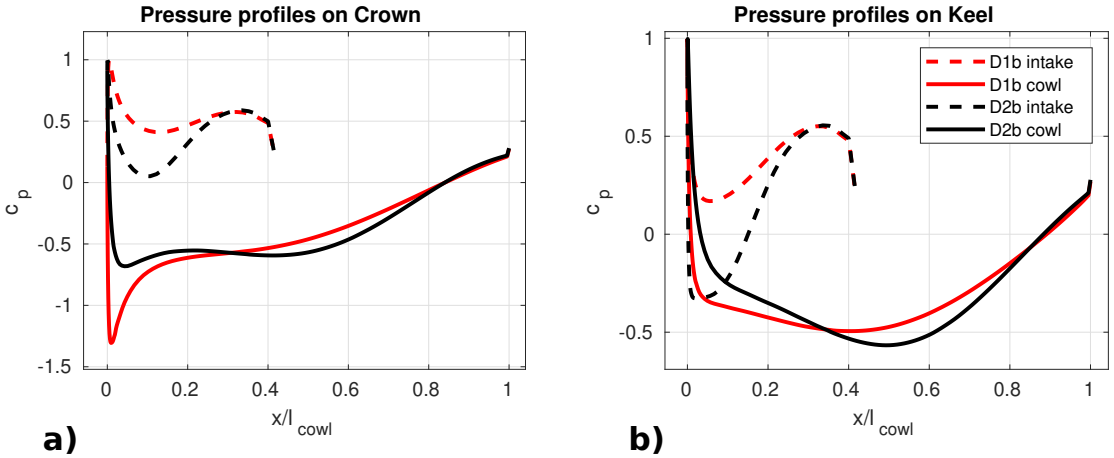

Figure 4.11: Pressure distribution on intake and cowl profiles for crown and keel positions.

Although the highly cambered D2b shows good flow attachment near the crown, as seen in fig. 4.11b, a relatively steeper adverse pressure gradient was observed on the keel intake profile. This trend in c_p is not desirable as it increases the chance of flow separation for high AoAs, indicated by the aforementioned acceleration bubble in fig. 4.10b. The performance metrics and the force budget for configuration drag are shown in table 4.3 and the fig. 4.12 establishes the normalized configuration drag budget for designs D1b and D2b.

Table 4.3: Performance criteria from 3-D axisymmteric analysis

Design	c_d^* (projected)	$F_{net}/(qA_{eff})$ (Axial)	MFCR
D1b	1	0.4595	0.6745
D2b	1.0413	0.4570	0.7776

c_d^* normalized based on D1b

The reason for negative cowl force $\phi_{c,p}$ in design D1b is lip suction effect caused at by the local flow acceleration. Figure 4.10c shows an acceleration bubble in the design D1b on top of cowl. This creates a suction effect where the static pressure along the leading edge part of the cowl drops to relatively lower values compared to the cowl aft-body. Hence, a net forward force, opposite to the direction of flow is obtained when pressure forces are integrated on the cowl surface. As seen in fig. 4.12, the negative cowl force counteracts the increased pre-entry force for the design D1b. However, this may be mitigated with inlet drooping, where the intake profile is better aligned with the incoming flow. Doing so, local incidence effects can be mitigated, leading to reduced streamline curvature around the cowl lip.

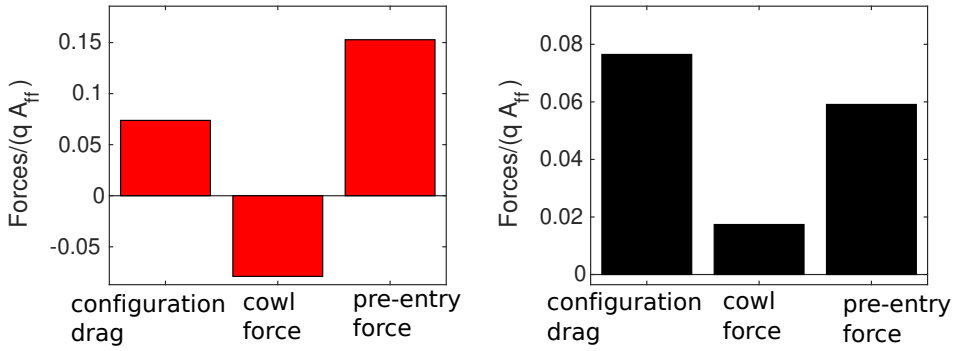

a) Force budget for Design D1 b) Force budget for Design D2

Figure 4.12: Configuration drag budget comparison between designs D1b and D2b.

To study the effect of inlet drooping, Design D1b was selected owing to reduced c_d and high η_i.

4.4.1.2 Asymmetric design performance study of D1 for cruise operation- Comparing D1b, D1c and D1d

The asymmetric design analysis starts off with studying the effect of drooping on design D1 (high spillage) for cruise operation. Two variants of D1b, which are D1c and D1d were defined by setting the inlet drooping angle θ_d to 2° and 4° respectively. The geometrically transformed inlet profiles at keel and crown positions are shown in fig. 4.13. With increasing θ_d, better flow alignment was observed.

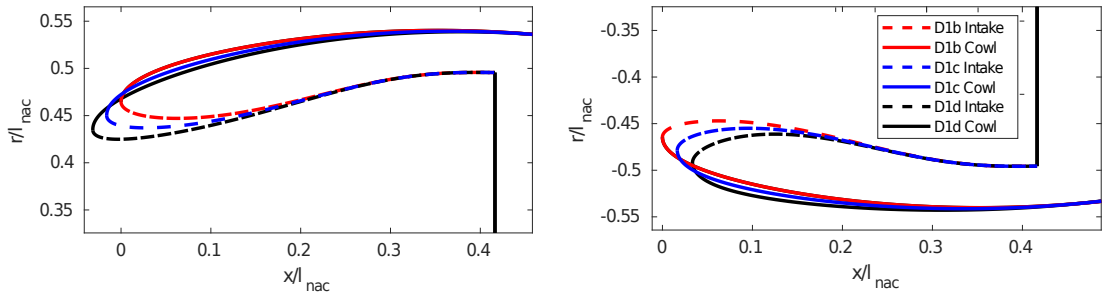

a) Crown profile transformation **b)** Keel profile transformation

Figure 4.13: Geometric representation of drooped profiles

The figures 4.14 and 4.15 show the pressure profiles and Mach no. contours respectively.

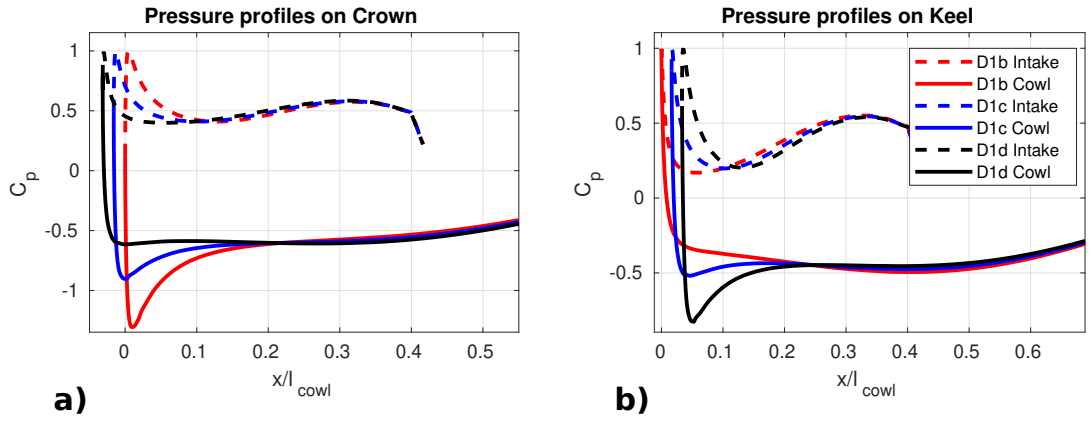

Figure 4.14: Pressure plots on crown and keel positions for varying θ_d.

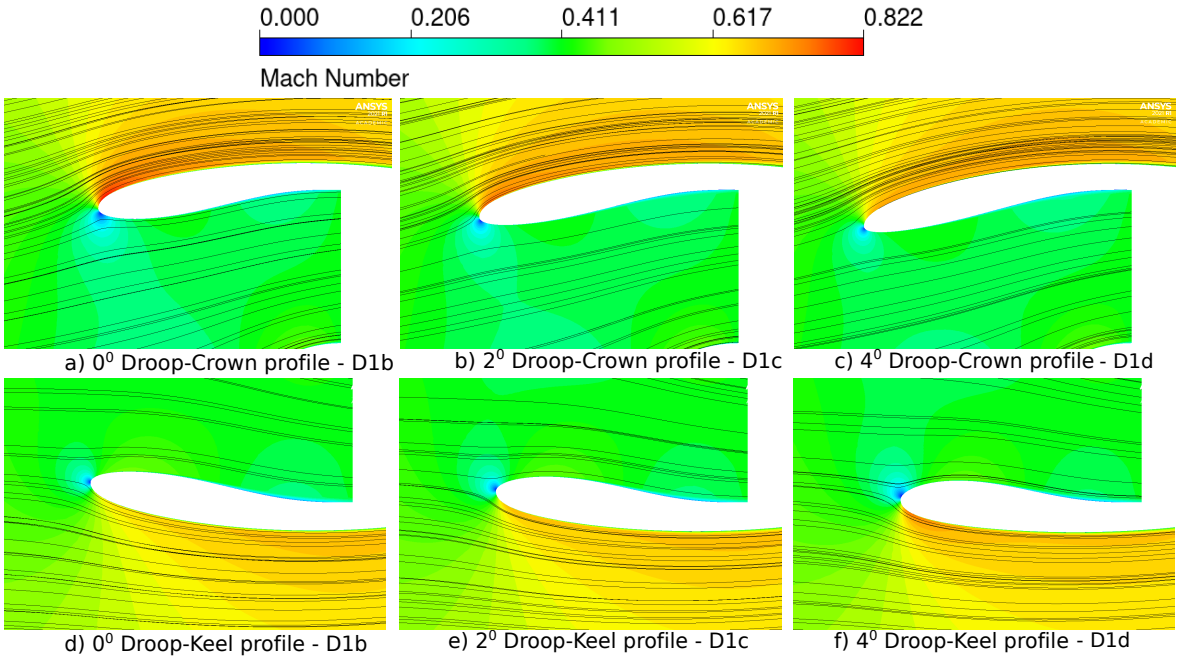

Figure 4.15: Mach no. contours at crown and keel positions for different θ_d.

Considering the crown position, the pressure plots in fig. 4.14a show how inlet drooping mitigates the sudden drop in pressure (c_p) on the cowl's leading edge position. This allows for a gradual change in the static pressure over the cowling and avoids sudden changes in streamline curvature. Design D1d with θ_d 4°, possess smooth pressure distribution on the crown profile, comparatively. Further, the Mach number contours in figs. 4.15a-c show, better flow alignment for design D1d and reduced streamline turning. The position of the stagnation point is of utmost importance as it decides the susceptibility to flow acceleration seen over the cowl profile. Design D1d, owing to its better flow alignment, has its stagnation point positioned close to the highlight position rather than on the intake side as seen in designs D1b and D1c. This forces the streamlines to take a longer route than usual, which is observed as an acceleration bubble in designs D1b and

D1c. Conversely, at the keel profile, a minor pressure drop was observed on the outer cowling with drooping as shown in fig. 4.14b. The geometric transformation thickens the keel profile, as seen in fig. 4.13b and this moves the stagnation point more towards the intake profile visualized in fig. 4.15d-f. Thus, there is an increased streamline curvature at keel with increased inlet drooping as seen from a pressure drop in fig. 4.14b. The inlet performance of the designs as a function of the inlet drooping is populated in table 4.4.

Table 4.4: Variations in intake performance as a function of θ_d

Droop angle [°]	0 (D1b)	2 (D1c)	4 (D1d)
c_d^*	1	0.9922	0.9855
η_i	0.999259	0.999267	0.999271

c_d^* normalized based on D1b

Although design D1d shows a minor acceleration bubble over cowl profile at keel, it allows for good flow alignment at crown. Further, design D1d shows almost 15% reduction in c_d at cruise, which is a crucial parameter considering fuel economy and also has better intake performance as seen from improved η_i.

4.4.2 Take-off rotation operating condition

The take-off (TO) rotation condition investigated in this section depicts the nacelle's aerodynamic performance at the end of the runway. The AoA for this case was set to 22°, which accounts for the aircraft pitch and also the wing up-wash effects. The take-off condition is a critical operation point on the flight envelope that tests for intake separation. The various design variants of D1 that were analyzed at the take-off condition are presented in the table 4.5. The design T1 used in the TO analysis is the high spillage D1 design introduced in the previous sections. The designs T2, T3 and T4 are the derivatives of design T1 with increasing θ_d. While, designs T5 and T6 have profile modifications done at keel profile relative to design T4.

Table 4.5: Description of cases studied for nacelle's take-off performace

CASES	**T1**	**T2**	**T3**	**T4**	**T5**	**T6**
θ_d[°]	0	2	3	4	4	4
Increment to r_{hi}/r_{fan} at the keel profile [%]	0	0	0	0	1.5	3

r_{hi}/r_{fan} increments done relative to design T4

The findings were presented in two subsections where the effects of inlet drooping and design modifications done to keel are discussed thoroughly.

4.4.2.1 Aerodynamic effects of inlet drooping- Comparing T2, T3 and T4

Take-off performance of drooped designs T2, T3 and T4 were studied in this section. To check for the flow separation at lip, Mach no. contours were analyzed

and quantification of flow distortion was done with the use of DC_{60} parameter. The Mach no. contours and pressure plots depicting the performance of the keel profile are shown in figs. 4.16 and 4.17 respectively.

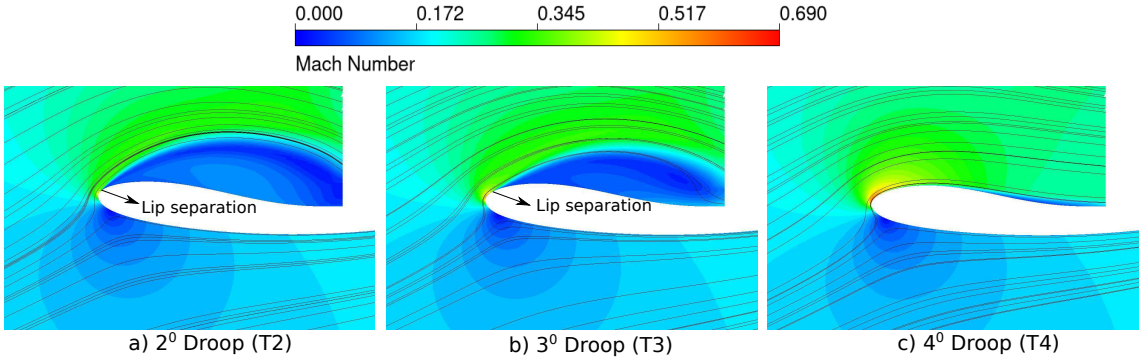

Figure 4.16: Comparing Mach no. contours at take-off condition for different θ_d.

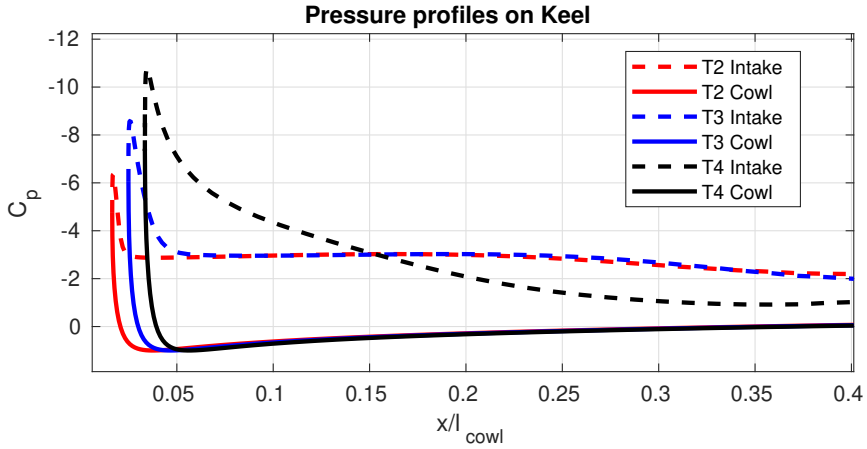

Figure 4.17: Obtained pressure profiles at take-off condition for different θ_d.

Comparing the Mach number contours and c_p profiles, inlet drooping facilitates better flow attachment near the lower part of the nacelle. In the current study, design T4 with $\theta_d = 4°$, had essentially mitigated flow separation. This is due to the fact that, the relatively thickened lip at keel profile in design T4 allows for a gradual variation in c_p along the intake as shown in fig. 4.17. The iso-surfaces of zero axial velocity are shown in fig. 4.18. Although zero axial velocity essentially indicates the separation boundary layer, $u_x = 0.5$ m/s iso-surfaces were processed for avoiding rough edges.

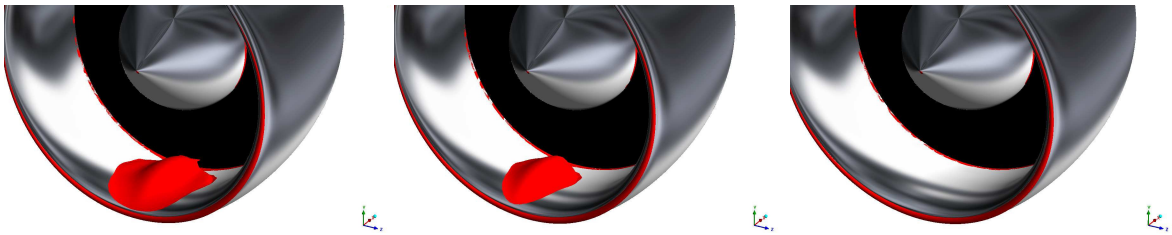

a) 2^0 Droop (T2) b) 3^0 Droop (T3) c) 4^0 Droop (T4)

Figure 4.18: Comparing Iso-surfaces of zero axial velocity at take-off consitions (AoA = 22°) for different θ_d.

The iso-surfaces are representative of the flow separation and demarcate the boundary of flow separation at the intake keel profile. The drooped design T4 shows no flow separation. Thus, inlet drooping helps with better flow alignment at cruise operation and results in reduced c_d. The engine parameters such as normalized $\dot{m}$ and fan pressure ratio PR_{fan} are tabulated in table 4.6.

Table 4.6: Take-off performance comparison with inlet drooping

Designs	$\dot{m}\ /\dot{m}_{des}$	DC_{60}	PR_{fan}/PR_{des}
T2	0.9919	0.138941	0.9977
T3	1.005	0.089274	1.0002
T4	1.0148	0.015793	1.0016

The results show that T4 has the lowest flow distortion at fan face, indicated by reduced DC_{60}. Engine mass ingestion in seen to increase with inlet drooping as flow separation was mitigated. This is due to the fact that, flow separation at the intake profile leads to flow blockage and subsequent reduction in the engine's air ingestion.

4.4.2.2 Aerodynamic effects due to Keel profile modification

To further reduce flow distortion at fan face due to lip separation, minor increment to the parameter r_{hi}/r_{fan} was done to the keel profile, and this resulted in better aerodynamic performance, flow attachment and lowered fan distortion. Design variants T5 and T6, derived from design T4 were studied to analyze fan distortion at fan face. Figures 4.23 and 4.20 show the Mach no. contours and pressure plots obtained at the keel profile.

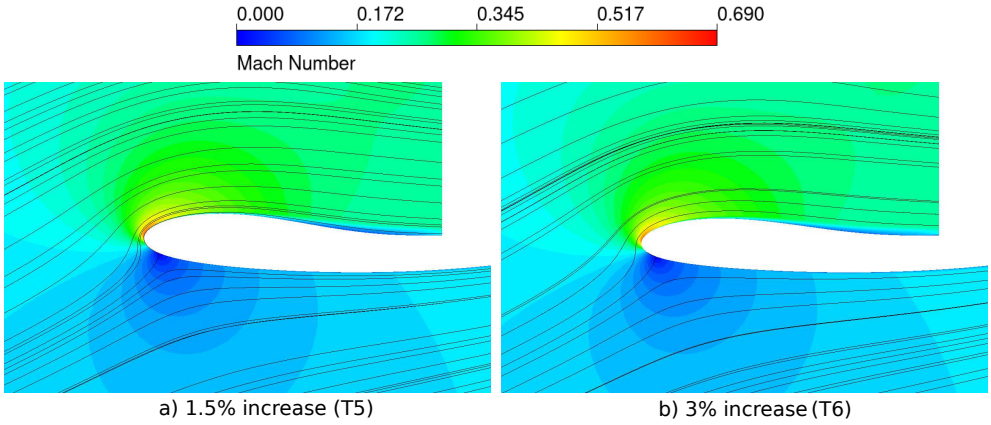

Figure 4.19: Comparing Mach. no plots for increased r_{hi}/r_{fan}.

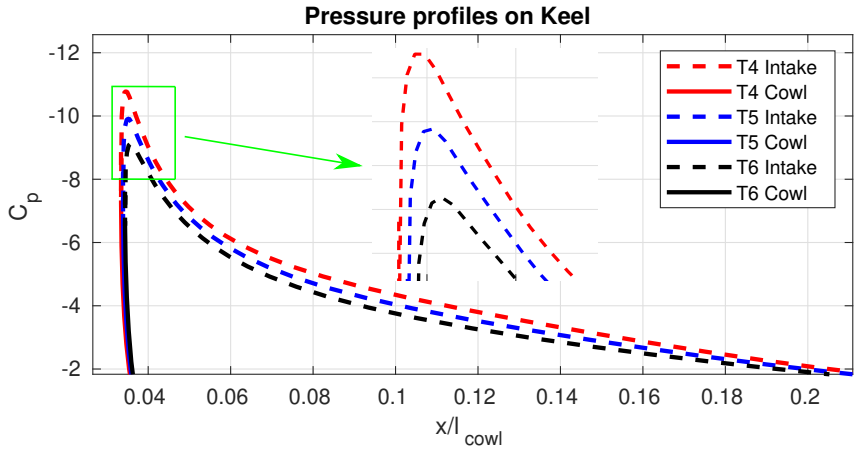

Figure 4.20: Comparing pressure profiles for increased r_{hi}/r_{fan}.

The pressure plot in fig. 4.20 clearly shows a reduced pressure drop for design T6 as the flow moves around the lip. However, the slope or the pressure plot remained unchanged indicating that the flow attachment characteristics weren't compromised. This resulted in a less intense acceleration bubble and streamline curvature as observed from the Mach number contours. Table 4.7 compares the flow distortion parameter DC_{60} and cruise drag for designs T4, T5 and T6.

Table 4.7: Take-off performance comparison with keel modification and cruise performance analysis

Designs	$\dot{m}/\dot{m}_{des}$	DC_{60}	PR_{fan}/PR_{des}	c_d^* at cruise
T4	1.0148	0.015793	1.0016	0.9855
T5	1.0152	0.014731	1.0017	0.9826
T6	1.0154	0.013330	1.0017	0.9806

c_d^* normalized based on D1b

The designs T4, T5 and T6, being successful candidates for the TO operation, were tested for cruise operation as well. Although the aerodynamic effects due

to increasing r_{hi}/r_{fan} is not appreciable in cruise conditions, considerable reduction in DC_{60} at TO condition was seen. For the TO operating conditions, design T5 and T6 show 6.72% and 15.59% reduction in flow distortion parameter DC_{60} estimated at fan face respectively. Meanwhile, minor improvements in cruise conditions were obtained as design T6 shows 0.5% reduction in c_d.

4.4.3 Crosswind operating condition

In this section, the design modifications and results pertaining to an operating point where significant crosswind flow at take-off condition were investigated. Although the design procedure for pure crosswind case could have resulted in a more robust design, a crosswind case during takeoff was deemed beneficial to study the lip separation effects. Aircraft certification protocols necessitate that the engine should be stable and operable during take-off and landing whilst experiencing pure crosswinds (crosswind flow at 90° to the nacelle), for a minimum wind velocity of 20 knots [36].

4.4.3.1 CW case setup

A comparison of pure crosswind case with the investigated case setup is shown in fig. 4.21a and b respectively. An aggressive operation condition is the pure crosswind case where the engine has no axial velocity component. This case idealizes the starting of the engines experiencing pure crosswind at the beginning of the runway. This case tests the lip intake profiles to assess the crosswind performance like lip separation and flow distortions.

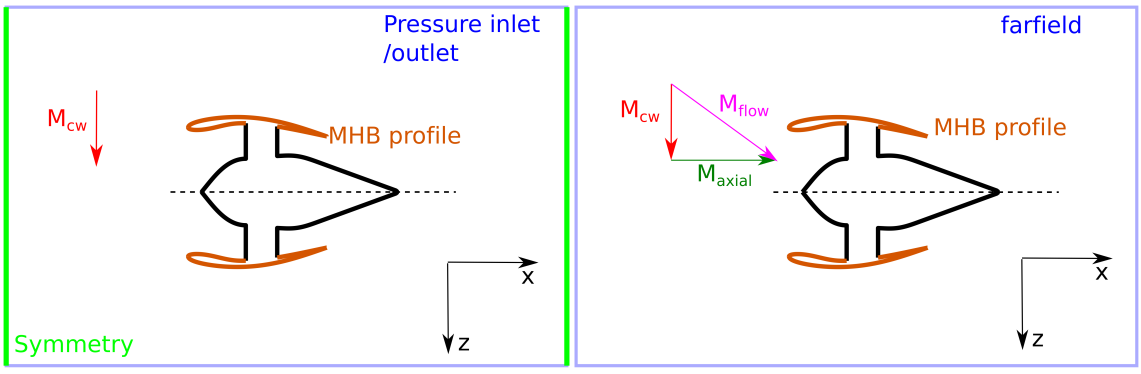

a) Pure crosswind b) Investigated case

Figure 4.21: Description of case setup for crosswind condition.

The crosswind case considering axial velocity component, shown in fig. 4.21b was chosen over the pure crosswind operation for the following reasons.

- Initial test cases with pure crosswind required modification of outer boundaries to pressure inlet/ outlet condition for better convergence. Yet, the flow convergence was not satisfactory.

- No engine performance data was available for an operating condition with a freestream Mach number equal to zero. An unrealistic operating condition would arise from using the same fan boundary conditions as the ones used for the fan at the end of runway.
- This aforementioned flow characteristics rendered the design modification ineffective and showed no improvement in mitigation of flow separation owing to the unrealistic operating condition.

To represent the operating conditions seen at the runway's end, an axial Mach number (M_{axial}) corresponding to the TO condition with 0° AoA was chosen. This assumption was consistent with the fan speed line and operating point data provided by GKN aerospace, as the problems mentioned, which are unrealistic engine mass flow and insensitivity of the flow field towards profile modifications, were mitigated.

4.4.3.2 Profile modifications to MHB and crown profiles

For the crosswind flow analysis, design T6, the best design from the TO condition, was chosen as the initial design. For a strong crosswind condition, flow separation is expected to occur on the windward side of the intake profile that spans almost from the keel to the crown profile circumferentially [32]. For the present nacelle design with a conventional intake length, only minor modifications to the MHB profile and crown profile were adequate to mitigate intake lip separation. The crosswind test done on design T6 showed a fairly non-trivial zone of flow separation positioned in-between the MHB and crown profiles but bordering on the MHB profile. This can be visualized in fig. 4.24a. Intuitively, this could be understood that the MHB profile requires a focused shape profile modification as it changes the nacelle's side geometry to maintain an attached flow during crosswinds. The modifications made to the keel profile for design T6 during climb operation resulted in no flow separation on the lower quarter, spanning from MHB to keel profile on the windward side, during the crosswind test. Based on the aforementioned discussions, the parameters that were modified for this study are presented in table 4.8. The following table compares the design modifications made to MHB parameters that resulted in two new derivatives termed CW1 and CW2.

Table 4.8: Design modifications done to MHB and crown profiles for crosswind analysis

Designs	**Crown profile Modification (% increment)**	**MHB profile modification (% increment)**			
	$f_{le,c}$, $f_{le,I}$	CR	AR_{lip}	$f_{le,c}$, $f_{le,I}$	r_{hi}/r_{fan}
T6	0	0	0	0	0
CW1	1.5	0.5	0.5	1.5	1.25
CW2	1.5	1	1	2.5	1.5

Profile modifications in % increments with reference to design T6

The non-dimensionalized lip radii corresponding to the cowling and the inlet

profile, $f_{le,c}$ and $f_{le,I}$ were subjected to a modest increment of 1.5% to maintain attached flow on the windward side close to the MHB position. The lip aspect ratio AR_{lip} of design CW1 was increased by 0.5% relative to design T6 so as to allow for a gradual change in the diffuser curvature. Thus, the susceptibility of flow separation is reduced as this design accounts for reduction in adverse pressure gradient effects. The lip contraction ratio, a parameter that modifies the lip thickness is increased by 0.5% and 1% for designs CW1 and CW2 respectively. This thickens the lip and facilitates better flow attachment characteristics. The highlight radius is increased at the MHB position as it helps with repositioning of the flow stagnation point which avoids abrupt changes in streamline curvature. MHB profile shapes for the base design T6 and its derivatives CW1 and CW2 are shown in fig. 4.22.

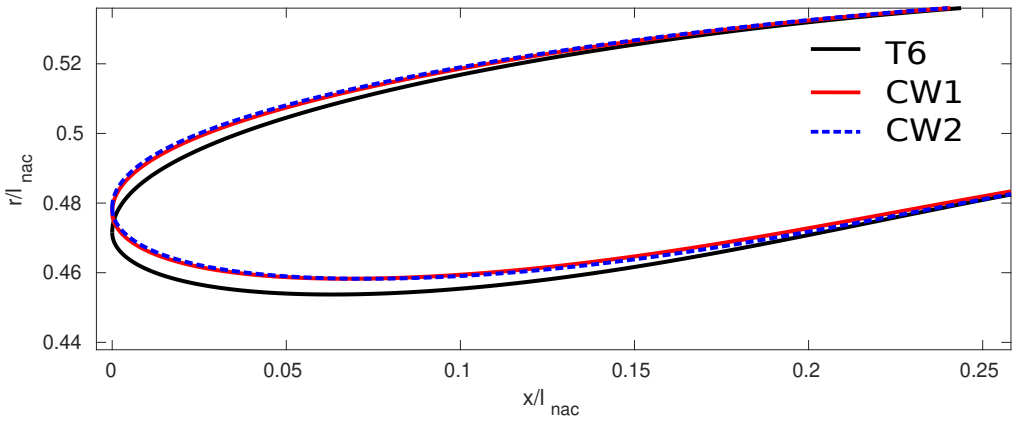

Figure 4.22: MHB profiles for the base and modified designs.

Although it's hard to visualize the difference between the CW1 and CW2 profiles, upon careful inspection, the lip's thickness and length is considerably higher for CW2 compared to CW1.

4.4.3.3 Distortion parameter for crosswind operation

Crosswind test on design T6 showed a flow separation near adjoining MHB profile as seen in fig. 4.24a. To quantify the flow distortion effects with DC_{60} parameter, the annular sector spanning 60° had to be positioned to house the separation zone. The geometric details of the new annular sector is presented in fig 4.23.

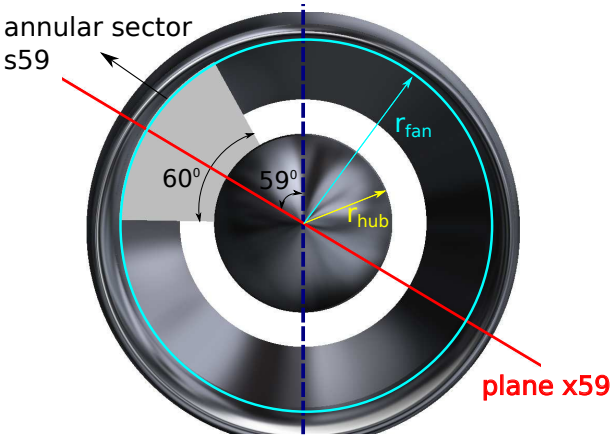

Figure 4.23: Schematic of the annular sector and contour plane for crosswind analysis.

As seen in the figure 4.23, the sector s59 is symmetrically positioned about a line that has 59° inclination relative to the vertical axis. The sector was imprinted on the fan face so as to obtain the local area-averaged total pressure for evaluating DC_{60} parameter. To visualize the flow separation through Mach number contours, a plane termed x59, defined co-planar to x axis and with an inclination of 59° with the vertical axis was defined as shown in fig. 4.23. The iso-surfaces representing zero axial velocity ($u_x = -0.1m/s$) and the Mach number contours are shown in figs. 4.24 and 4.25 respectively.

Figure 4.24: Comparing iso-surfaces of zero axial velocity to assess crosswind performance.

The Mach number contours for design T6 shows a considerable flow separation trend and an intense recirculation zone. The profile modifications done to the MHB profile resulted in a thicker lip and repositioning of the flow stagnation point, allowing for better flow attachment. Figure 4.26 shows the C_p plot on the curve defined by the intersection of the cowling profile and the plane x59.

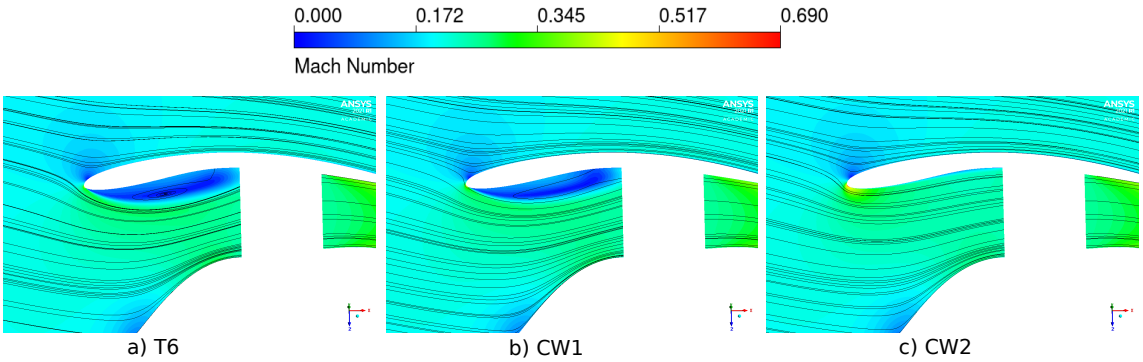

Figure 4.25: Mach number contours plotted on plane x59.

Although the initial profile modification that resulted in design CW1 doesn't show appreciable mitigation of flow separation, design CW2 succeeded in maintaining an attached flow throughout the inlet. A gradual change in the pressure profile along the intake surface was seen in design CW2. This trend was quite not present in its predecessors CW1 and T6.

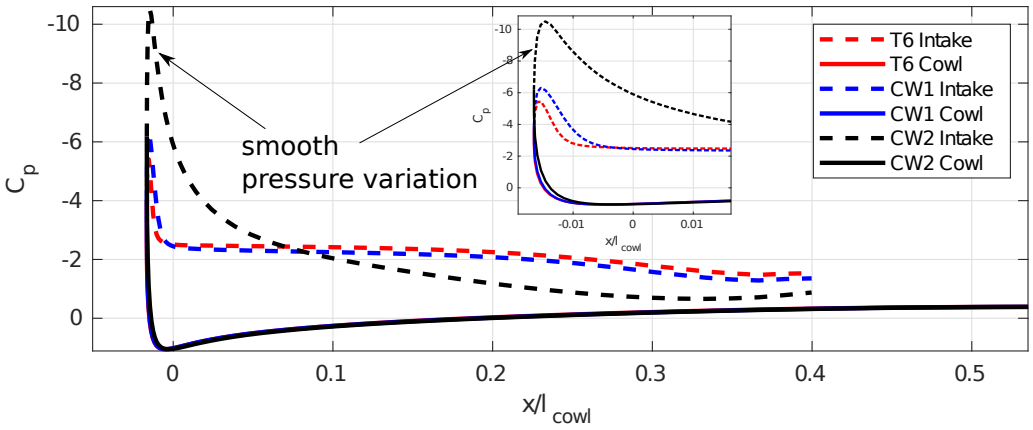

Figure 4.26: Pressure distribution plotted on nacelle profile-plane x59 intersection curve.

The obtained DC_{60} parameter and the corresponding c_d at cruise operation are presented in table 4.9. The designs CW1 and CW2 were again tested for cruise operation to evaluate their c_d. Design CW2 shows the least flow distortion at take-off operation. Comparing the three designs for cruise operation shows a considerable increase in c_d as a result of inlet profile modification.

Table 4.9: Crosswind performance comparison and cruise analysis

Designs	DC_{60}	c_d^* at cruise
T6	0.0804	0.9806
CW1	0.0617	0.9834
CW2	0.0078	0.9842

c_d^* normalized based on D1b

Design CW2, the best design from the CW analysis shows 0.37% increase in c_d compared to the best design for take-off, T6. However, this trivial increase in cruise drag is a minor trade off considering the enhanced crosswind performance. Further, considering the initial axisymmetric design D1b, the modified design T6 shows 1.6% reduction in cruise drag.

5
Conclusion

Initially, to select the best nacelle for cruise operation, multi-objective design optimization studies were carried out separately for the nacelle and nozzle profiles on selected optimization parameters. The parametric optimization process was based on 2-D axisymmetric CFD analysis and a non-dominated sorting genetic algorithm (NSGA-II).The selection of a baseline design was based on the nacelle's objective functions and the aerodynamic performance parameters. The results from the 2-D axisymmetric optimization studies, visualized from the Pareto diagrams and the performance parameters, aided in selecting the optimal design as the baseline design. Based on the initial 2-D and 3-D CFD analysis done on the spinner design, considering the parameters c_d and η_i, a sharp pointed spinner with 51° HCA was selected.

From the 2-D optimization studies, 2 baseline designs, D1 and D2 with contrasting intake profiles were selected and analyzed, among which the high-spillage intake design D1 was selected owing to its reduced c_d. Subsequently, a multi-point 3-D aerodynamic design study was conducted to modify the baseline nacelle D1 to ensure that it maintains attached flow at all operating conditions, which are, cruise, take-off, and crosswind. In cruise operation, the aerodynamic effects of inlet drooping were investigated. The design with a 4°droop angle at the intake demonstrated better flow alignment and, as a result, lower c_d. Furthermore, for the TO operation, local profile modifications were investigated, and subsequent cruise analysis for the modified design revealed an even lower c_d as a result of a change in intake force budget. The crosswind performance of the nacelle at the end of the runway was studied by tweaking MHB and keel profiles, which resulted in a final design CW2 that maintained attached flow, as determined by estimation of DC_{60}, streamlines, and velocity iso-surface.

The results appeared to be fruitful, as the finalized design CW2 demonstrated good aerodynamic performance in crosswind conditions while only adding a trivial 0.5% to c_d during cruise operation with respect to design T6. When compared to design D1b, design CW2 still shows a reduced c_d by 1.5%.

Bibliography

[1] ES Van der Sman, B Peerlings, J Kos, R Lieshout, and T Boonekamp. Destination 2050. 2020.

[2] MA Cameron, MZ Jacobson, Steven RH Barrett, Haitao Bian, Chieh-Chieh Chen, Sebastian D Eastham, A Gettelman, A Khodayari, Q Liang, HB Selkirk, et al. An intercomparative study of the effects of aircraft emissions on surface air quality. *Journal of Geophysical Research: Atmospheres*, 122(15):8325–8344, 2017.

[3] Rui Qiu, Shuhua Hou, Xin Chen, and Zhiyi Meng. Green aviation industry sustainable development towards an integrated support system. *Business Strategy and the Environment*, 30(5):2441–2452, 2021.

[4] David S Lee and Piers Forster. Guest post: Calculating the true climate impact of aviation emissions.

[5] A. Frassoldati, A. Cuoci, T. Faravelli, E. Ranzi, S. Colantuoni, P. Di Martino, and G. Cinque. Experimental and modeling study of a low nox combustor for aero-engine turbofan. *Combustion Science and Technology*, 181(3):483–495, 2009.

[6] A Broglia, L Clozza, M Russo, C Spada, L Vendemini, AG Zuanetti, Carlo Riboldi, and Lorenzo Trainelli. Flynk-the future all-electric commuter concept for metropolitan areas. In *24th Conference of the Italian Association of Aeronautics and Astronautics (AIDAA 2017)*, pages 1–10, 2017.

[7] Thomas H Bradley, Blake A Moffitt, Dimitri N Mavris, and David E Parekh. Development and experimental characterization of a fuel cell powered aircraft. *Journal of Power sources*, 171(2):793–801, 2007.

[8] Mark D Guynn, Joshua E Freh, and Erik D Olson. Evaluation of a hydrogen fuel cell powered blended-wing-body aircraft concept for reduced noise and emissions. Technical report, 2004.

[9] Dries Verstraete. Long range transport aircraft using hydrogen fuel. *International journal of hydrogen energy*, 38(34):14824–14831, 2013.

[10] GKN Aerospace to lead development of Electric Fan Thruster for electric aircraft gkn aersopace `https://bit.ly/3dr0EG6`,.

[11] Anders Lundbladh, H Martensson, A Petrusson, et al. Installation effects for ultra-high bypass engines. In *23rd ISABE Conference, Manchester, UK*, 2017.

[12] Matthew H Robinson, David G MacManus, Alexander Heidebrecht, and Nicholas Grech. An optimisation method for nacelle design. In *55th AIAA Aerospace Sciences Meeting*, page 0708, 2017.

[13] Andreas Peters, Zoltán S Spakovszky, Wesley K Lord, and Becky Rose. Ultrashort nacelles for low fan pressure ratio propulsors. *Journal of turbomachinery*, 137(2):021001, 2015.

[14] Nagabhushana Rao Vadlamani, Teng Cao, Rob Watson, and Paul G Tucker. Toward future installations: Mutual interactions of short intakes with modern high bypass fans. *Journal of Turbomachinery*, 141(8):081013, 2019.

[15] Yongjian Zhong and Songyang Li. A 3d shape design and optimization method for natural laminar flow nacelle. In *Turbo Expo: Power for Land, Sea, and Air*, volume 50770, page V001T01A024. American Society of Mechanical Engineers, 2017.

[16] Roland Wilhelm. An inverse design method for engine nacelles and wings. *Aerospace science and technology*, 9(1):19–29, 2005.

[17] Fernando Tejero, David G MacManus, and Christopher Sheaf. Surrogate-based aerodynamic optimisation of compact nacelle aero-engines. *Aerospace Science and Technology*, 93:105207, 2019.

[18] Kalyanmoy Deb, Amrit Pratap, Sameer Agarwal, and TAMT Meyarivan. A fast and elitist multiobjective genetic algorithm: Nsga-ii. *IEEE transactions on evolutionary computation*, 6(2):182–197, 2002.

[19] Cornelis P Van Dam. Recent experience with different methods of drag prediction. *Progress in Aerospace Sciences*, 35(8):751–798, 1999.

[20] D Destarac and J Van Der Vooren. Drag/thrust analysis of jet-propelled transonic transport aircraft; definition of physical drag components. *Aerospace science and technology*, 8(6):545–556, 2004.

[21] Florian R Menter. Two-equation eddy-viscosity turbulence models for engineering applications. *AIAA journal*, 32(8):1598–1605, 1994.

[22] Inc Ansys. Ansys fluent theory guide. *Canonsburg, Pa*, 794, 2011.

[23] William T Cousins and Milt W Davis Jr. Evaluating complex inlet distortion with a parallel compressor model: part 1—concepts, theory, extensions, and limitations. In *Turbo Expo: Power for Land, Sea, and Air*, volume 54617, pages 1–12, 2011.

[24] Milt W Davis Jr and William T Cousins. Evaluating complex inlet distortion with a parallel compressor model: Part 2—applications to complex patterns. In *Turbo Expo: Power for Land, Sea, and Air*, volume 54617, pages 13–23, 2011.

[25] Vinícius Tavares Silva. *Aerodynamic Design and Experimental Investigation of Short Nacelles for Future Turbofan Engines*. PhD thesis, Chalmers Tekniska Hogskola (Sweden), 2020.

[26] Brenda Kulfan and John Bussoletti. " fundamental" parameteric geometry representations for aircraft component shapes. In *11th AIAA/ISSMO multidisciplinary analysis and optimization conference*, page 6948, 2006.

[27] Robert Christie, Alexander Heidebrecht, and David MacManus. An automated approach to nacelle parameterization using intuitive class shape transformation curves. *Journal of Engineering for Gas Turbines and Power*, 139(6), 2017.

[28] MS Zawislak, DJ Cerantola, and AM Birk. Identifying opportunities for reducing nacelle drag. *Journal of Engineering for Gas Turbines and Power*, 140(2), 2018.

[29] Linkai Li, Yang Liu, and Hui Hu. An experimental study on dynamic ice accretion process over the surfaces of rotating aero-engine spinners. *Experimental Thermal and Fluid Science*, 109:109879, 2019.

[30] Cesare A Hall and Daniel Crichton. Engine design studies for a silent aircraft. 2007.

[31] Dennis L Berry. The boeing 777 engine/airframe integration aerodynamic design process. In *ICAS PROCEEDINGS*, volume 19, pages 1305–1305. AMERICAN INST OF AERONAUTICS AND ASTRONAUTICS, 1994.

[32] Vinícius T Silva, Anders Lundbladh, Olivier Petit, and Carlos Xisto. Multipoint aerodynamic design of ultrashort nacelles for ultrahigh-bypass-ratio engines. *Journal of Propulsion and Power*, pages 1–18, 2022.

[33] Timothy L Crawford, Ronald J Dobosy, and Edward J Dumas. Aircraft wind measurement considering lift-induced upwash. *Boundary-Layer Meteorology*, 80(1):79–94, 1996.

[34] Vance A Tucker. Gliding birds: reduction of induced drag by wing tip slots between the primary feathers. *Journal of experimental biology*, 180(1):285–310, 1993.

[35] Hairun Xie, Yadong Wu, Anjenq Wang, and Hua Ouyang. Numerical investigation of inlet distortion for different rear mounted engine installations at taking-off conditions. In *Turbo Expo: Power for Land, Sea, and Air*, volume 56628, page V001T01A009. American Society of Mechanical Engineers, 2015.

[36] GWH van Es. Crosswind certification-how does it affect you? 2006.

A

Appendix 1

A.1 Comparative study of fan face boundary condition for take-off operation

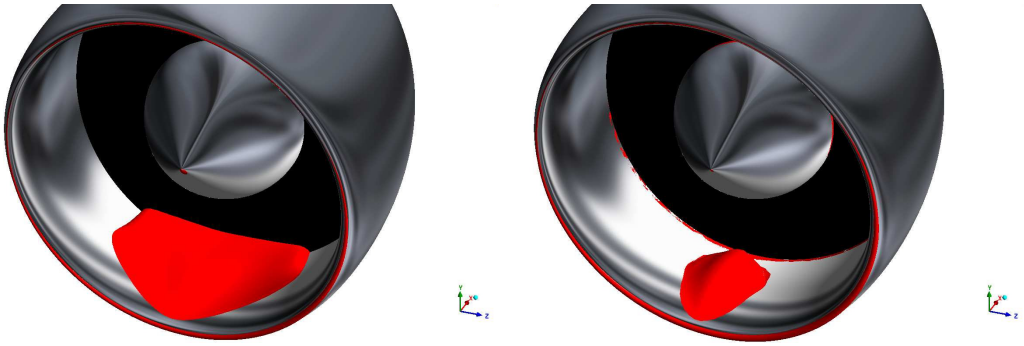

a) Constant pressure outlet boundary b) MPC method to set pressure profile

Figure A.1: Iso-surfaces of $u_x = 0$ to denote flow separation in the intake profile .

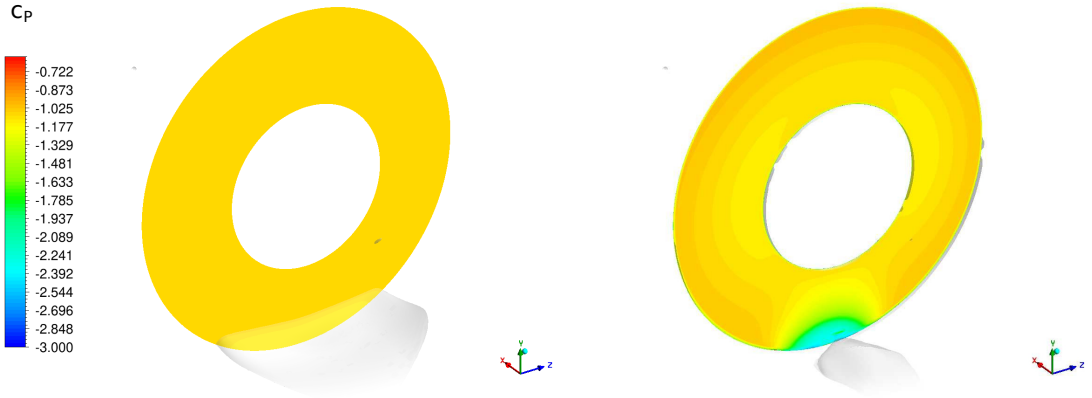

a) Constant pressure outlet boundary b) MPC method to set pressure profile

Figure A.2: Pressure coefficient (C_P) contour on fan face.

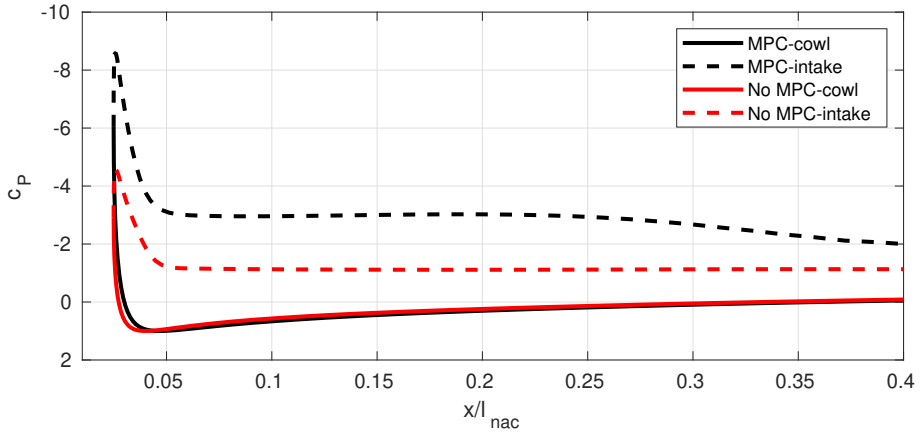

Figure A.3: comparison of pressure profiles at the keel position.

DEPARTMENT OF SOME SUBJECT OR TECHNOLOGY
CHALMERS UNIVERSITY OF TECHNOLOGY
Gothenburg, Sweden
www.chalmers.se

CHALMERS
UNIVERSITY OF TECHNOLOGY